



**HAL**  
open science

# Detection of turbulence occurrences from temperature, pressure, and position measurements under superpressure balloons

Richard Wilson, Clara Pitois, Aurélien Podglajen, Albert Hertzog, Miléna Corcos, Riwal Plougonven

## ► To cite this version:

Richard Wilson, Clara Pitois, Aurélien Podglajen, Albert Hertzog, Miléna Corcos, et al.. Detection of turbulence occurrences from temperature, pressure, and position measurements under superpressure balloons. *Atmospheric Measurement Techniques*, 2023, 16, pp.311-330. 10.5194/amt-16-311-2023 . insu-03741063v2

**HAL Id: insu-03741063**

**<https://insu.hal.science/insu-03741063v2>**

Submitted on 29 Jan 2023

**HAL** is a multi-disciplinary open access archive for the deposit and dissemination of scientific research documents, whether they are published or not. The documents may come from teaching and research institutions in France or abroad, or from public or private research centers.

L'archive ouverte pluridisciplinaire **HAL**, est destinée au dépôt et à la diffusion de documents scientifiques de niveau recherche, publiés ou non, émanant des établissements d'enseignement et de recherche français ou étrangers, des laboratoires publics ou privés.



Distributed under a Creative Commons Attribution - NonCommercial 4.0 International License



# Detection of turbulence occurrences from temperature, pressure, and position measurements under superpressure balloons

Richard Wilson<sup>1</sup>, Clara Pitois<sup>1</sup>, Aurélien Podglajen<sup>2</sup>, Albert Hertzog<sup>2</sup>, Milena Corcos<sup>2</sup>, and Riwal Plougonven<sup>2</sup>

<sup>1</sup>LATMOS-IPSL, Sorbonne Université, Paris, France

<sup>2</sup>LMD-IPSL, École polytechnique, Palaiseau, France

**Correspondence:** Richard Wilson (richard.wilson@latmos.ipsl.fr)

Received: 8 June 2022 – Discussion started: 5 July 2022

Revised: 17 December 2022 – Accepted: 22 December 2022 – Published: 20 January 2023

**Abstract.** This article deals with the detection of small-scale turbulence from in situ meteorological measurements performed under superpressure balloons (SPBs). These balloons allow long-duration flights (several months) at a prerequisite height level. The data set is gathered from the Strateole-2 probationary campaign during which eight SPBs flew in the tropical tropopause layer at altitudes of around 19 and 20.5 km from November 2019 to March 2020.

Turbulence is not directly measured by the instrument set onboard the SPBs. Nonetheless, there is the potential to derive information about the occurrence of turbulence from the temporally well-resolved measurements of pressure, temperature, and position. It constitutes a challenge to extract the aforementioned information from a measurement set that was not designed for quantifying turbulence, and the paper explains the methodology developed to overcome this difficulty.

It is observed that SPBs oscillate quasi-periodically around their equilibrium positions. The oscillation periods, which are 220 s on average with a range of 130 to 500 s, are close to but noticeably smaller than the Brunt–Väisälä period ( $\sim 300$  s). The amplitude of these vertical motions is  $\sim \pm 15$  m, inducing large fluctuations in all quantities, whether measured (e.g., pressure, temperature and position) or inferred (e.g., density and potential temperature). The relationships between the changes in these quantities and the vertical displacements of the balloons are used to infer properties of the flow in which the SPBs drift.

In the case of active turbulence, the vertical stratification as well as the wind shear are likely to be reduced by mixing. Hence, the increments of potential temperature,  $\delta\theta$ , and of the vertical displacements of the balloon,  $\delta z_B$ , are expected

to be uncorrelated because  $\partial\theta/\partial z \rightarrow 0$ . Moreover, the local vertical gradients of measured quantities, temperature ( $T$ ) and horizontal velocities ( $u$  and  $v$ ), are estimated from the covariance of the increments of the considered quantity with  $\delta z_B$ . The Richardson number of the flow is deduced.

Several binary indexes (true or false) to describe the state of the flow, laminar or turbulent, are evaluated. These turbulence indexes, based either on correlations between  $\delta\theta$  and  $\delta z_B$  or on estimates of the local Richardson number, are found to be consistent, as they differ in less than 3 % of cases. The flow is observed to be turbulent for about 5 % of the time, with strong inhomogeneities along the longitude.

## 1 Introduction

The vertical transport of heat, momentum, and minor constituents in the tropical upper troposphere–lower stratosphere (UTLS) is an important issue, as this region is recognized as the gateway for tropospheric air into the stratosphere (Fueglistaler et al., 2009). Above 15 km altitude, this vertical transport is believed to mainly result either from the mean tropical upwelling associated with the Brewer–Dobson circulation or from small-scale turbulence. The relative contribution of turbulent mixing to this vertical transport is highly uncertain, partly owing to the lack of observations. Turbulence observations in the tropical UTLS are indeed sparse: they mostly come from two large very high frequency (VHF) radars, from relatively few radiosondes, or from research aircraft.

From measurements of the Equatorial Atmospheric Radar (EAR), located in West Sumatra (0.20° S, 100.32° E), In-

onesia, Fujiwara et al. (2003) observed intermittent turbulence near the tropical tropopause with significant enhancements (a factor of 5) in the turbulent kinetic energy (TKE) lasting several days. Such enhancements in the TKE are believed to result from the breaking of large-scale Kelvin waves. Using the same EAR data set, Yamamoto et al. (2003) showed that eastward vertical wind shear around the equatorial tropopause frequently generates turbulence through Kelvin–Helmholtz instabilities (KHIs). Mega et al. (2010) presented detailed structures of KHIs in the equatorial UTLS from both high-resolution EAR measurements (using an interferometric imaging method) and radiosondes. From the VHF radar located in Gadanki (13.5° N, 79.2° E), India, Satheesan and Murthy (2002) and Satheesan and Krishna Murthy (2004) described turbulence characteristics in the tropical UTLS. These authors estimated TKE and TKE dissipation rates using several methods. Interestingly, they did not observe a clear variability in the turbulence intensity within the UTLS with altitude.

Sunilkumar et al. (2015) and Muhsin et al. (2016) presented the characteristics of turbulence in the tropical UTLS from GPS radiosonde observations obtained during more than 3 years at two stations located on the Indian Peninsula: Trivandrum (8.5° N, 76.9° E) and Gadanki (13.5° N, 79.2° E). The turbulent layers were detected using Thorpe’s analysis (Thorpe, 1977) and following the procedure proposed by Wilson et al. (2010, 2011, 2013). The statistics of various turbulence parameters as well as the Brunt–Väisälä frequencies and the vertical shears are described for the convective troposphere and for the UTLS. The parameters describing the turbulence are either directly measured, such as the Thorpe lengths (an outer scale of turbulence) and the frequency of appearance of unstable layers, or are inferred on the basis of physical assumptions, like the TKE dissipation rates and the eddy diffusivity. Muhsin et al. (2020) extended the two previous studies by analyzing the soundings of six stations in South India, adding the Cochin (10° N, 76.3° E), Coimbatore (10.9° N, 76.9° E), Goa (15.5° N, 73.8° E), and Hyderabad (17.5° N, 78.6° E) stations to the two previously mentioned. These data were acquired during 4 years, from August 2013 to December 2017. All of these studies, based on radiosondes measurements, consistently show that the probability of occurrence of instability, either estimated from the gradient Richardson number ( $Ri$ ) or from the squared Brunt–Väisälä frequency ( $N^2$ ), decreases with altitude above an altitude of 15 km, i.e., in the UTLS. They found that the probability of occurrence for  $Ri$  to be less than 0.25 is between 0% and 5% in the height range from 18 to 25 km and that the probability of occurrence of unstable regions ( $N^2 < 0$ ) is quasi-null. Interestingly, Muhsin et al. (2016) did not observe a clear diurnal cycle in the tropical UTLS.

Many studies of turbulence in the free atmosphere have been based on measurements from research aircraft (see Dörnbrack et al., 2022, and references therein); however, to our knowledge, only one study has involved the tropical

UTLS. Podglajen et al. (2017) used high-resolution (20 Hz) airborne measurements to study the occurrence and properties of small-scale ( $\lesssim 100$  m) wind and temperature fluctuations in the tropical UTLS over the Pacific Ocean. They showed that wind fluctuations are very intermittent and appear to be localized in shallow layers, typically with  $\sim 100$  m thickness. Furthermore, active turbulent events appear to be more frequent at relatively low altitude and near deep convection. They observed that the motions are close to 3D isotropic and that the power spectra follow a  $\sim -5/3$  power law scaling. The diffusivity induced by turbulent bursts is estimated to be in the order of  $10^{-1} \text{ m}^2 \text{ s}^{-1}$  and decreases from the bottom to the top of the tropical UTLS.

Apart from convective regions, many observations of the free atmosphere show successions of strata, i.e., alternating layers in which the flow is turbulent, whose depth varies from a few tens to a few hundreds of meters, separated by stable static regions, i.e., regions where the flow is laminar (e.g., Luce et al., 2015; Podglajen et al., 2017; Wilson et al., 2018). The numerical simulations of Fritts et al. (2003) support such observations. Turbulent and laminar strata are expected to exist in the tropical UTLS. As turbulence, by nature, is a dissipative process, the turbulent layers have a finite lifetime, depending on the mesoscale processes yielding energy (shear instability or wave breaking). Thus, by observing the flow at a given altitude level, we expect to find an alternation of turbulent and laminar episodes.

The Strateole-2 project has been set up in recent years in order to better understand the dynamics, transport, microphysics, and dehydration of the tropical UTLS (Haase et al., 2018). It is an international project involving several research groups, mostly in France and the USA, led by the Laboratoire de Météorologie Dynamique (LMD) and Centre National d’Études Spatiales (the French space agency). The uniqueness and strength of the Strateole-2 project come from the fact that the atmospheric measurements are obtained under superpressure balloons (SPBs) that can fly for several months (typically 3 months) at an approximately constant density level. Standard measurements performed under all of the Strateole-2 SPBs, including temperature, pressure, and GPS position, allow one to describe meso- and small-scale dynamic processes at the flight level, in a quasi-Lagrangian way (Hertzog and Vial, 2001; Hertzog et al., 2012; Podglajen et al., 2016; Corcos et al., 2021). The SPBs usually carry a second gondola with several configurations of instruments, allowing measurements of constituents, aerosols, cloud heights, and radiation, among others.

The main purpose of this paper is to present the methods allowing one to determine the dynamical state of the flow, laminar or turbulent, in which the SPBs are flowing. It is based on the estimation of the local stratification of the flow using measurements of temperature, pressure, and GPS position. The rest of the paper is organized as follows: the data set used is presented in Sect. 2, the methods for detecting turbulence and for estimating various indicators of the flow

**Table 1.** Main characteristics of Strateole-2 C0 flights. All superpressure balloons are equipped with TSEN (Thermodynamics SENSors) instruments.

Flight ID	Height (m)	Launch date (UT)	Duration (days)
01_STR1	20 652	12 November 2019	107
02_STR2	20 502	11 November 2019	103
03_TTL3	19 110	18 November 2019	101
04_TTL1	18 780	27 November 2019	66
05_TTL2	18 800	5 December 2019	79
06_STR1	20 380	6 December 2019	57
07_STR2	20 125	6 December 2019	83
08_STR2	20 100	7 December 2019	77

stability are described in Sect. 3, some results are presented (Sect. 4) and discussed (Sect. 5), and a concluding section (Sect. 6) summarizes the main findings of the paper.

## 2 The data set

### 2.1 The Strateole-2 C0 campaign

The probatory Strateole-2 campaign, called Strateole-2 C0, was held from November 2019 to March 2020. During this campaign, eight SPBs were launched from Mahé (4°37' S, 55°27' E), Seychelles, and flew eastward following the quasi-biennial oscillation (QBO) phase that prevailed in the lower stratosphere at this time (Fig. 1). The main characteristics of the flights are provided in Table 1. Four of these flights carried only the TSEN (Thermodynamics SENSors) instrument and its associated GPS receiver, whereas the other four carried additional scientific instruments. At first order, SPBs fly at a quasi-constant density level (Vincent and Hertzog, 2014). TTL and STR flights were associated with different carried masses and/or balloon sizes, and they drifted at altitudes of  $\sim 19$  and  $\sim 20.5$  km, respectively.

### 2.2 The TSEN measurements

In this study, we use the TSEN measurements that are performed at the balloon flight level for each flight. They consist of two respective temperature measurements, one with a thermistor sensor ( $T_S$ ) and one with a thermocouple sensor ( $T_C$ ), and a pressure measurement ( $P$ ). They are closely associated with GPS observations that provide the position (long; lat; and altitude above sea level, a.s.l.) of the balloon as well as with the solar zenith angle (SZA). All of these measurements are acquired every 30 s, except for the pressure measurements that are acquired every 1 s.

These raw measurements enable us to compute two estimates of the balloon potential temperature ( $\theta_S$  and  $\theta_C$ ) and density ( $\rho_S$  and  $\rho_C$ ), respectively, obtained with the thermistor and thermocouple temperatures. The horizontal velocity

components ( $u$  and  $v$ ) are evaluated from successive GPS positions.

In the following, we will make use of the increments of measured quantities, namely the differences between consecutive measurements:  $\delta T_S$  will, for instance, stand for the increments of the thermistor temperatures. Note that two independent estimates of the balloon vertical displacements are available: (1)  $\delta z_{GPS}$  obtained with the raw GPS altitudes and (2)  $\delta z_P$  computed with the pressure measurements and further assuming hydrostaticity.

TSEN measurements were also performed on the profiling unit of the Reel-down Aerosol Cloud Humidity and Temperature Sensors (RACHuTS) instrument (Kalnajs et al., 2021). RACHuTS notably allows one to obtain vertical temperature profiles of 2 km length below the balloon by reeling down (and then up) the profiling unit at a vertical velocity of about  $1 \text{ m s}^{-1}$ . Only one TSEN temperature sensor (a thermistor) is implemented in the profiling unit. Measurements are performed with a nominal sampling rate of 1 Hz, i.e., the vertical resolution of the RACHuTS temperature profiles is  $\sim 1$  m. We degraded its vertical resolution to about 30 m in order to (1) improve upon the 1 m raw precision of altitude measurements and (2) obtain a similar vertical resolution from TSEN and RACHuTS measurements (as the amplitude of the balloon oscillations is typically  $\pm 15$  m).

### Instrumental noise

The instrumental noise of the TSEN measurements is an important characteristic that has to be taken into account to assess whether the flow is turbulent. It is assumed that this noise is a zero-mean, uncorrelated process, i.e., a white noise, contributing to the measured signal. A way to estimate the white noise level is to compute the variance of the  $n$ th-order increments of the time series ( $n \gtrsim 6$ ), such as high-order differentiation performing a high-pass filtering of the time series. As shown in Appendix A, the variance of the  $n$ th-order increments tends to the variance of the uncorrelated signal weighted by the sum of the squared binomial coefficients of order  $n-1$ . Here, noise levels are estimated on time segments of 21 samples (10 min); thus, they are estimated on more than 10 000 segments for a flight lasting  $\sim 100$  d. This method works well if the signal spectra exhibit a quasi-constant floor, i.e., if white noise clearly contributes to the measured signal for frequencies smaller than the Nyquist frequency, as is frequently the case for lidar or radar signals. However, we do not observe any white noise level for the TSEN measurements acquired with a sampling period of 30 s ( $T_S, z, u$ ) (see, for instance, the power spectra of the vertical displacements  $\delta z$  shown in Fig. 6). Therefore, the variance of the  $n$ th-order increments cannot be interpreted as being solely due to uncorrelated noise, even if some noise is expected to contribute to this high-frequency variance. However, a rough estimate of the noise level has been evaluated from the data segments showing the smallest variances, i.e., segments for which a

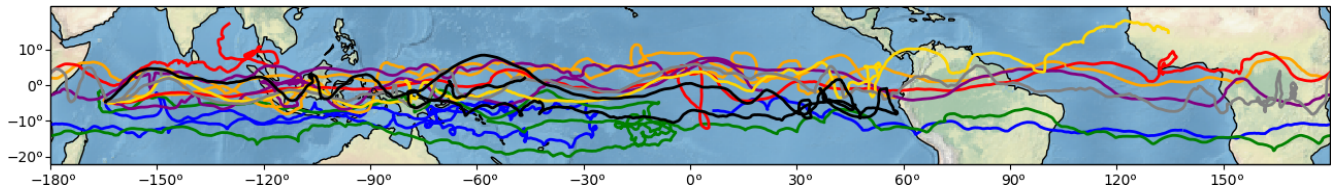


**Figure 1.** Trajectories of the eight SPBs.

**Table 2.** Estimated noise (standard deviation) of temperature, pressure, and dry potential temperature. For each flight, the first row indicates the flight-mean values (bold), and the second row indicates the respective nighttime and daytime average values.

	$T_S$ (mK)	$T_C$ (mK)	$P$ (Pa)	$\theta_S$ (mK)	$\theta_C$ (mK)
01_STR1	<b>7</b> 5, 27	<b>7</b> 5, 22	<b>0.1</b> 0.08, 0.12	<b>17</b> 12, 64	<b>17</b> 13, 75
02_STR2	<b>2</b> 1, 6	<b>2</b> 2, 6	<b>0.05</b> 0.04, 0.06	<b>5</b> 3, 15	<b>5</b> 4, 15
03_TTL3	<b>14</b> 8, 36	<b>10</b> 7, 23	<b>0.12</b> 0.11, 0.15	<b>31</b> 19, 78	<b>21</b> 15, 52
04_TTL1	<b>9</b> 6, 31	<b>8</b> 6, 23	<b>0.17</b> 0.15, 0.18	<b>19</b> 13, 67	<b>16</b> 12, 50
05_TTL2	<b>3</b> 2, 7	<b>3</b> 2, 9	<b>0.06</b> 0.05, 0.07	<b>6</b> 4, 16	<b>6</b> 4, 20
06_STR1	<b>6</b> 4, 26	<b>6</b> 5, 25	<b>0.08</b> 0.07, 0.09	<b>13</b> 9, 62	<b>15</b> 11, 60
07_STR2	<b>5</b> 4, 18	<b>7</b> 5, 23	<b>0.09</b> 0.08, 0.12	<b>12</b> 9, 42	<b>16</b> 12, 54
08_STR2	<b>3</b> 2, 8	<b>3</b> 2, 8	<b>0.06</b> 0.05, 0.07	<b>7</b> 5, 20	<b>7</b> 6, 20

comparatively smaller contribution of the atmospheric signal is expected. Tables 2 and 3 display estimates of the noise levels for quantities measured or inferred, obtained with the average of the smallest 10 % of variance values of the sixth-order increments. Such estimates, although not fully satisfying, nevertheless provide valuable information on the relative quality of the data, allowing one to compare noise levels between sensors, between flights, or between night and day measurements.

The noise levels of the two temperature sensors, the thermocouple and thermistor, are quasi-identical. We note that the noise level of temperature measurements is a factor of 3–5 larger during daytime than during nighttime for all flights. Such an increase in temperature noise during the day very likely results from the random passage of the sensors in the wake of their electrical wires or mechanical support. These devices, which are significantly thicker than the sensors themselves, are heated by solar radiation during daytime

**Table 3.** Same as Table 2 but for altitudes derived from the pressure and altitude observations as well as zonal and meridional velocities.

	$z_P$ (m)	$z_{GPS}$ (m)	$u$ (cm s <sup>-1</sup> )	$v$ (cm s <sup>-1</sup> )
01_STR1	<b>0.11</b> 0.10, 0.14	<b>0.32</b> 0.29, 0.36	<b>0.2</b> 0.2, 0.3	<b>0.2</b> 0.2, 0.3
02_STR2	<b>0.05</b> 0.04, 0.07	<b>0.10</b> 0.1, 0.120	<b>0.1</b> 0.1, 0.1	<b>0.1</b> 0.1, 0.1
03_TTL3	<b>0.11</b> 0.10, 0.13	<b>0.26</b> 0.24, 0.27	<b>0.2</b> 0.2, 0.3	<b>0.2</b> 0.2, 0.3
04_TTL1	<b>0.14</b> 0.13, 0.15	<b>0.32</b> 0.30, 0.33	<b>0.3</b> 0.2, 0.3	<b>0.2</b> 0.2, 0.3
05_TTL2	<b>0.05</b> 0.05, 0.06	<b>0.12</b> 0.12, 0.13	<b>0.1</b> 0.1, 0.2	<b>0.1</b> 0.1, 0.1
06_STR1	<b>0.09</b> 0.08, 0.10	<b>0.28</b> 0.27, 0.30	<b>0.6</b> 0.5, 0.7	<b>0.2</b> 0.2, 0.2
07_STR2	<b>0.10</b> 0.09, 0.13	<b>0.27</b> 0.26, 0.29	<b>0.2</b> 0.2, 0.2	<b>0.2</b> 0.2, 0.2
08_STR2	<b>0.07</b> 0.06, 0.08	<b>0.27</b> 0.23, 0.31	<b>0.1</b> 0.1, 0.1	<b>0.1</b> 0.1, 0.1

and are consequently warmer than the air or even the sensor temperature. We also observe that the flight 03\_TTL3 temperature measurements are the noisiest (14 mK vs. 2–9 mK). Unlike the other flights, during which temperature sensors were hanging at the very bottom of the flight train as far as possible from large elements (e.g., the gondolas), sensors on flight 03\_TTL3 were located within the flight train. Thus, they were more prone to be affected by the warm wake of other devices in the flight train during daytime.

The noise estimates with respect to the pressure measurements and to the vertical position measurements (from both pressure differences and GPS) are slightly larger during daytime than during nighttime. The reason for this slight increase in the noise level is probably not the consequence of an increase in instrumental noise. It may rather be the consequence of the greater amplitudes of the balloon oscillations during daytime, which would impact the energy density of  $P$  and  $z$  at high frequency. The noise levels of the horizontal wind components estimated from GPS positions are very

small, less than  $1 \text{ cm s}^{-1}$ . They do not show any night–day difference.

### 2.3 Oscillating movements of the balloons around their equilibrium positions

Superpressure balloons drift with the winds, following a quasi-Lagrangian behavior, which is useful to document the detailed evolution of a given air mass. Their displacements, however, differ from those of an air parcel in at least two ways. First and most importantly, the balloons follow isopycnic trajectories. The balloon envelope is almost inextensible, with the balloon diameter varying by less than 1%; hence, the volume is fixed as long as a superpressure is present. As the total mass of the flight train is fixed, the density of the balloon remains constant, implying an isopycnic trajectory. In contrast, air parcels follow isentropic trajectories in the absence of diabatic forcing. The second difference comes from the existence of natural oscillations of the balloon around its equilibrium density surface (EDS), where it achieves neutral buoyancy. These oscillations are of minor importance for the study of phenomena on timescales larger than a few tens of minutes (Vincent and Hertzog, 2014). However, they will be central to the current study, as an oscillating balloon samples short vertical profiles of key meteorological variables. The methodology developed in the present study precisely aims at exploiting these short “unintended” vertical profiles to diagnose the occurrence of turbulence.

The atmospheric density ( $\rho$ ) at the flight level is estimated from the measurements of temperature ( $T$ ) and pressure ( $P$ ) using the ideal gas law:  $\rho = P/R_a T$ , where  $R_a$  is the ideal gas constant for dry air per unit mass. As two independent measurements of  $T$  exist, two estimates of  $\rho$  can be calculated, denoted as  $\rho_S$  and  $\rho_C$ , using the thermistor or thermocouple temperatures, respectively. Figure 2 displays the systematic balloon fluctuations in density about their EDS (Fig. 2a), as well as the related variations in balloon altitudes (Fig. 2b) during 4 h of flight 01\_STR1. The fluctuations in density are about  $\pm 5 \times 10^{-4} \text{ kg m}^{-3}$ , corresponding to relative fluctuations of  $\sim \pm 0.5\%$ . The corresponding amplitude of the balloon vertical displacements is  $\pm 20 \text{ m}$  in this case. Thus, SPBs move around their EDS, exploring the atmosphere a few tens of meters above and below their position. These oscillatory motions induce fluctuations in the measured ( $P$ ,  $T$ ,  $z_{\text{GPS}}$ ) and inferred quantities ( $\rho$ ,  $\theta$ ,  $z_P$ ). We shall use these variations to describe some properties of the flow by hypothesizing that the observed variability in a quantity depends on both the balloon vertical displacement and the local vertical gradient in the quantity.

#### Periods and amplitudes of the vertical oscillations

Three angular frequencies, which are close to each other, first need to be distinguished: the Brunt–Väisälä frequency ( $N$ ), the neutral buoyant oscillation frequency ( $\omega_{\text{NBO}}$ ), and the ob-

served frequency of SPB oscillations ( $\omega_B$ ). The frequency at which a spherical balloon with constant volume oscillates about its EDS, the neutral buoyant oscillation (NBO) frequency, reads as follows (Hanna and Hoecker, 1971; Nasstrom, 1980; Vincent and Hertzog, 2014):

$$\omega_{\text{NBO}}^2 = \frac{4\pi^2}{t_{\text{NBO}}^2} = \frac{2g}{3T} \left( \frac{\partial T}{\partial z} + \frac{g}{R_a} \right), \quad (1)$$

where  $t_{\text{NBO}}$  is the NBO period, and  $g$  is the acceleration of gravity. The squared Brunt–Väisälä (BV) frequency,  $N^2 = g/T(\partial T/\partial z + g/c_p)$ , can be expressed as a function of  $\omega_{\text{NBO}}^2$ :

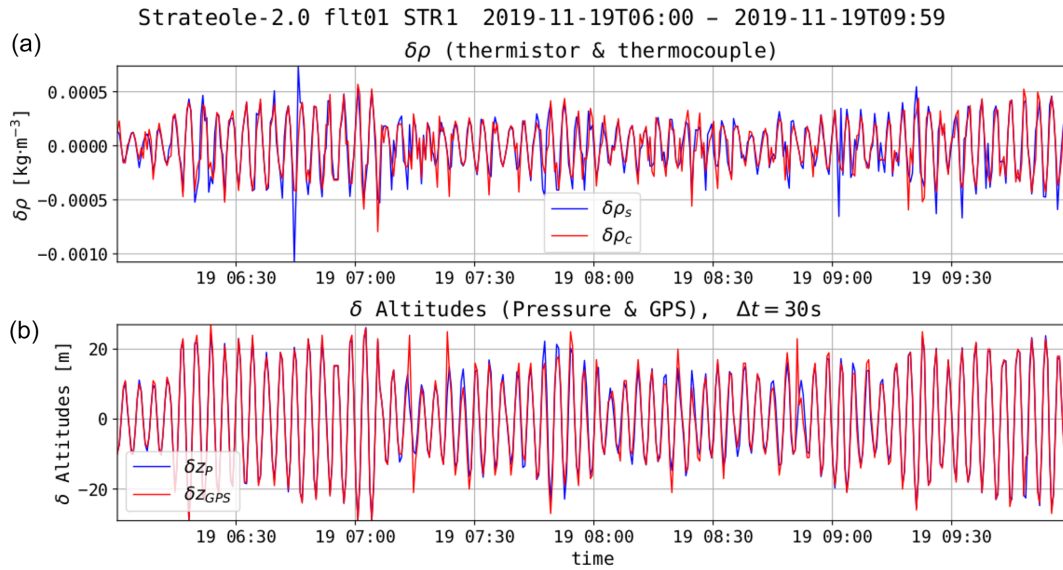
$$N^2 = \frac{3}{2}\omega_{\text{NBO}}^2 - \frac{g}{\gamma H} = \frac{3}{2}\omega_{\text{NBO}}^2 - \frac{5}{7}\frac{g}{H}, \quad (2)$$

where  $c_p$  is the air specific heat capacity at constant pressure,  $\gamma$  is the heat capacity ratio, and  $H = R_a T/g$  is the atmospheric scale height.

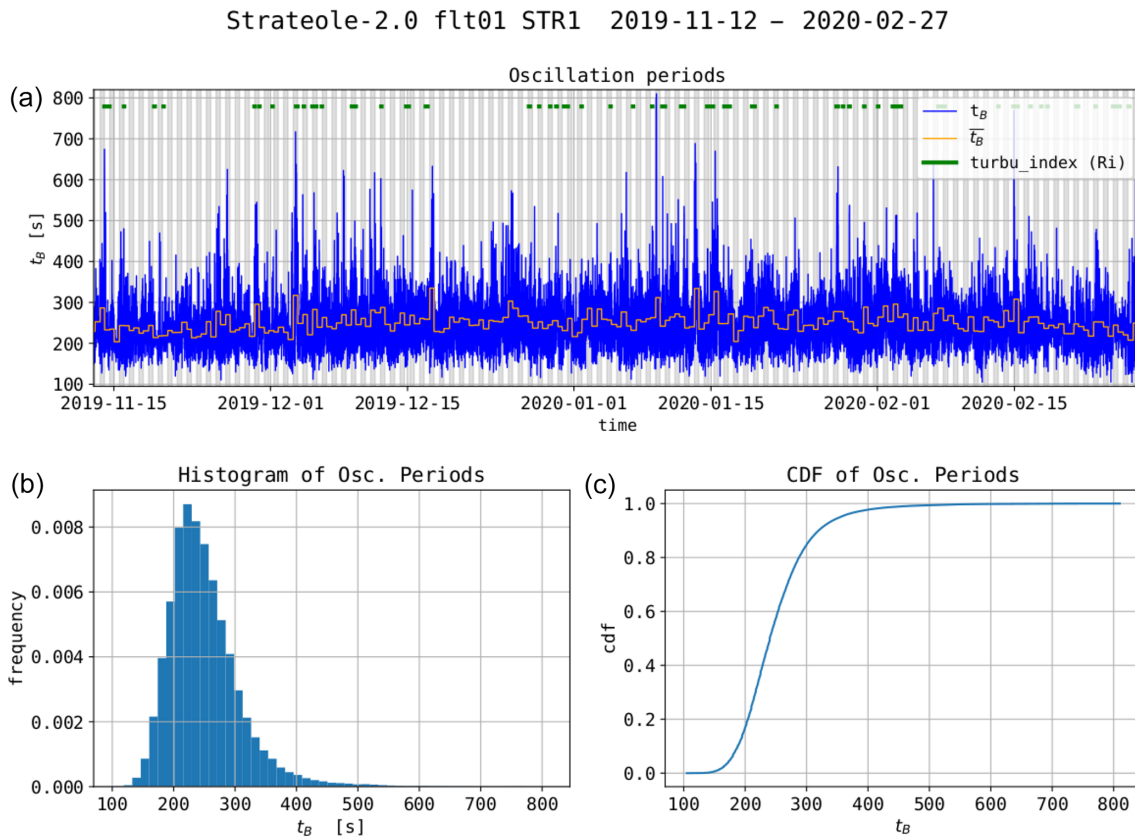
From Eq. (2), it can be shown that  $N \leq \omega_{\text{NBO}}$  as long as  $\omega_{\text{NBO}}^2 \leq 10g/7H$ , i.e.,  $t_{\text{NBO}} \geq 2.8\pi^2 H/g \approx 120 \text{ s}$ , or  $\partial T/\partial z \leq 8g/7R_a \approx 39 \text{ K km}^{-1}$ . Such conditions are met very frequently in the lower stratosphere, if not always. Note that both  $\omega_{\text{NBO}}$  and  $N$  increase with the vertical gradient of temperature  $\partial T/\partial z$ .

Figure 3a displays the observed periods of the balloon vertical oscillations ( $t_B$ ) for the whole 01\_STR1 flight. The gray and white stripes correspond to nights and days, respectively, and the orange curve shows the daytime and nighttime averages. The histogram of the oscillation periods is shown in Fig. 3b, and the periods are observed to range from  $\sim 135$  to  $800 \text{ s}$ . No clear day–night variation is visible. Figure 3c shows the cumulative distribution function (CDF) of the periods: the median  $t_B$  value is close to  $220 \text{ s}$ , and the mean is  $\sim 250 \text{ s}$ . Hence,  $\omega_B$  is larger than  $N$  as long as  $N$  is smaller than  $\approx 2.5 \times 10^{-2} \text{ rad s}^{-1}$ , which is a typical value in the tropical lower stratosphere. In the following, we shall see that  $\omega_B$  is systematically larger than  $N$ .

Figure 4 shows the corresponding amplitudes of the observed balloon oscillations as well as their probability and cumulative distribution function. The observed amplitudes range from  $\sim 0$  to  $150 \text{ m}$ , with an average (median) of  $14 \text{ m}$  ( $15 \text{ m}$ ). Some large amplitude oscillations ( $> 100 \text{ m}$ ) are observed. We found that they are most often associated with depressurization events. A weak but clear day–night variability is found: the oscillation amplitudes are about 20% larger during daytime than during nighttime. Moreover, greater variability in altitude is observed during daytime at high frequencies, as reported in Table 3.



**Figure 2.** (a) Density fluctuations observed from 06:00 to 10:00 UTC on 19 November. (b) Fluctuations in the height of the balloon for the same time interval.



**Figure 3.** (a) Estimates of the SPB oscillation periods during flight 01\_STR1; the orange staircase curve shows daytime and nighttime averages. (b) Histogram of the oscillation periods. (c) Cumulative distribution function of the oscillation periods.



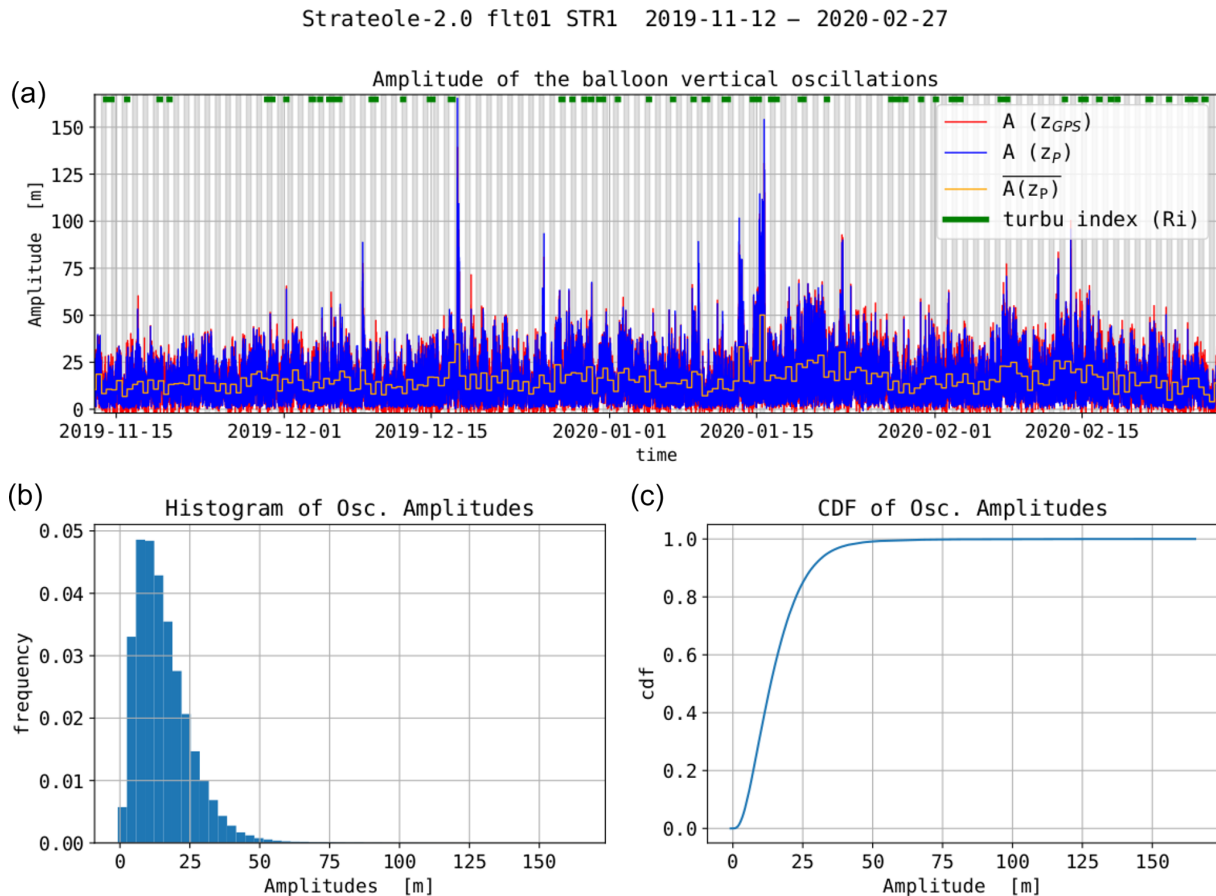


**Figure 4.** (a) Estimates of SPB oscillation amplitudes during flight 01\_STR1; the orange staircase curve shows daytime and nighttime averages. (b) Histogram of the oscillation amplitudes. (c) CDF of the oscillation amplitudes.

### 3 Data processing

#### 3.1 Methods for detecting the occurrence of turbulence from the TSEN measurements

The timescales of the turbulent fluctuations are expected to be smaller than the Brunt–Väisälä period,  $t_N$ . (In the following, “high frequencies” refer to frequencies larger than  $N/(2\pi)$ .) As  $t_B$  is close to or even smaller than  $t_N$ , the high-frequency variability up to the Nyquist frequency ( $1/60$  Hz) will be dramatically affected by the balloon oscillations regardless of the state of the flow (laminar or turbulent). Hence, the detection of turbulence from either the variance or the spectral characteristics of the TSEN measurements at high frequencies appears difficult, if not impossible.

Diagnostics on the dynamical state of the flow can, therefore, only be based on the local properties of atmospheric stratification, either stable or neutral/unstable. A consequence of turbulence is to restore stability from a preceding unstable state of the flow, which is achieved by locally mixing the fluid. In this case, the conservative quantities (potential temperature, specific humidity, and momentum) are

expected to exhibit weak horizontal and vertical variability within the turbulent layer. Note that neutral or even unstable stratification conditions may precede turbulence, but such conditions cannot persist and will necessarily cause turbulence. Conversely, laminar flow is expected to exhibit significant variability in the same quantities along the vertical direction.

The first way to diagnose that the flow is turbulent is, thus, to detect a null gradient in potential temperature. In such a case, the correlation between the vertical displacements ( $\delta z_B$ ) and the corresponding potential temperature increments ( $\delta\theta$ ) is expected to be null. Therefore, the implementation consists of testing the  $H_0$  hypothesis of a null correlation between  $\delta z_B$  and  $\delta\theta$ . This method is hereafter called the correlation method. The second way to diagnose a turbulent flow is based on the estimation of the local Richardson number  $Ri = N^2/S^2$ , where  $S^2 = (\partial u/\partial z)^2 + (\partial v/\partial z)^2$  is the squared shear. The flow is assumed to be turbulent when the Richardson number becomes less than 0.25. This method is hereafter called the  $Ri$  method.



### 3.2 Implementation of the two methods of turbulence detection

#### 3.2.1 Relationship between the increments of measured quantities and the increments of vertical displacements

The two proposed methods of turbulence detection are based on either estimates of correlations (for the correlation method) or linear regressions (for the Richardson method) between increments. The increments are simply defined as the differences between consecutive measures, separated by  $\delta t = 30$  s. Such a differentiation realizes a high-pass filtering of the time series. Both the correlations and the linear regressions are computed over time periods of 1 h, i.e., with 120 observations that are 30 s long. The choice of this number of observations enables one to obtain relatively small uncertainties on the estimates of correlation coefficients and slopes, at the price of being unable to detect turbulence layers with timescales significantly shorter than 1 h (in the frame moving with the wind).

The oscillatory motions of SPBs at frequency  $\omega_B$  are not expected to occur on isentropic surfaces nor on isopycnic surfaces. If the vertical displacement of the balloon between two different times separated by  $\delta t = 30$  s is  $\delta z_B = z_2 - z_1$ , the change in the measured potential temperature  $\delta\theta$  depends on both  $\delta z_B$  and the vertical displacement of the atmosphere  $\delta\zeta_\theta$  during  $\delta t$ :

$$\delta\theta = \overline{\theta}_z(z_2 - z'_1) = \overline{\theta}_z(\delta z_B - \delta\zeta_\theta), \tag{3}$$

with  $\delta\zeta_\theta = z'_1 - z_1$  corresponding to the change in the height of the isentropic surface during  $\delta t$  (see Fig 5). Equation (3) must be modified for nonconservative quantities, such as temperature ( $T$ ) or horizontal velocities ( $u$  and  $v$ ), in order to take into account the change in the considered quantity during  $\delta t$  on the isentropic surface. For instance, the temperature increment reads as follows:

$$\delta T = \overline{T}_z \delta z_B - \left( \overline{T}_z + \frac{g}{c_p} \right) \delta\zeta_\theta. \tag{4}$$

Figure 6 shows the power spectral density (PSD) of the vertical displacements ( $\delta z_B$ ) for flight 02\_STR2, either estimated from the GPS altitudes ( $\delta z_{GPS}$ ) or from the pressure observations ( $\delta z_P$ ). Both PSDs look very similar over the whole frequency range. A large spectral peak, centered at  $\sim 4 \times 10^{-3}$  Hz, is observed on these PSDs. This spectral peak corresponds to the SPB oscillatory motions about their EDS with a period of  $\sim 220$  s, as described in Sect. 2.3. Apart from long-duration balloons, radar is one of the few techniques that is able to infer the air vertical velocity in the free atmosphere. Few radar-borne PSDs of the vertical velocity have been published (Ecklund et al., 1986; VanZandt et al., 1991; Satheesan and Murthy, 2002). They either show a weak enhancement at frequencies close to  $N$  with respect to

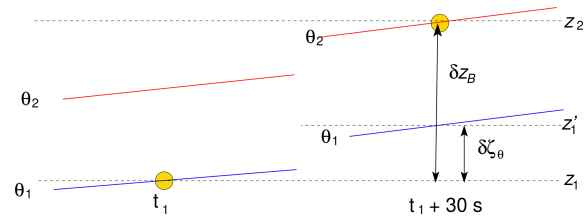


**Figure 5.** Schematic of the vertical displacement of an SPB. Between the measurement times  $t_1$  and  $t_1 + 30$  s, the vertical displacement of the SPB is  $\delta z_B$ , and the vertical displacement of the isentropic surface is  $\delta\zeta_\theta$ .

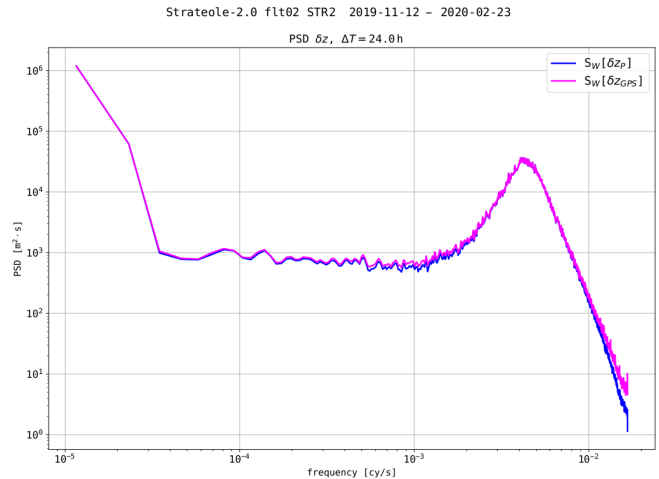


**Figure 6.** Power spectra of vertical increments of SPB heights, i.e., of vertical displacements between consecutive measurements (30 s), for flight 02\_STR2.

the spectral level at  $\omega \lesssim N$  or no enhancement at all. Thus, it is believed that the high-frequency vertical displacements in the balloon observations, 15 m on average, mostly result from the balloons’ oscillating motions about their EDS, rather than from the isentropic vertical displacements of air parcels. In other words,  $\delta z_B \gg \delta\zeta_\theta$  in Eqs. (3) and (4).

#### 3.2.2 The correlation method

The covariance of two quantities  $X$  and  $Y$ , is defined as follows:

$$\text{Cov}(X, Y) = E[(X - E[X])(Y - E[Y])].$$

Here,  $E$  is the mathematical expectation that is estimated by

$$\widetilde{\text{Cov}}(X, Y) = \frac{1}{N-1} \sum_{i=1}^N (X - \overline{X})(Y - \overline{Y}), \tag{5}$$

where  $N$  is the sample size. The Pearson correlation coefficient  $\rho_P(X, Y) = \frac{\text{Cov}(X, Y)}{\sigma_X \sigma_Y}$  is estimated as follows:

$$r_P(X, Y) = \frac{\widetilde{\text{Cov}}(X, Y)}{s_X s_Y}, \tag{6}$$

where  $s_X$  is the estimate of the standard deviation  $\sigma_X$  of quantity  $X$ , i.e.,  $s_X = \sqrt{\text{Cov}(X, X)}$ . A second correlation coefficient, the Spearman rank correlation coefficient,  $r_S(X, Y)$ , has also been used in the present study. It is a measure of the statistical dependence between the rank of two variables  $X$  and  $Y$ . It is computed as the Pearson correlation between the rank values of those two variables:

$$r_S(X, Y) = r_P(\text{rk}_X, \text{rk}_Y), \tag{7}$$

where  $\text{rk}_X$  is the rank of variable  $X$ , i.e., sample  $X$  is replaced by the rank of  $X$  in the expression of  $r_P$  (Eq. 6). The use of the nonparametric Spearman correlation makes it possible to get rid of outliers in the time series (Spearman, 1904).

If the flow is stably stratified, the increments of potential temperature  $\delta\theta$  are related to the vertical displacements of the SPB  $\delta z_B$  (Eq. 3). The covariance  $\text{Cov}(\delta\theta, \delta z_B)$  reads as follows:

$$\begin{aligned} \text{Cov}(\delta\theta, \delta z_B) &= E[\delta\theta \times \delta z_B] \\ &= E[\bar{\theta}_z (\delta z_B \times \delta z_B - \delta z_B \times \delta \zeta_\theta)]. \end{aligned} \tag{8}$$

Noting that (i)  $\delta \zeta_\theta \ll \delta z_B$  and (ii) the vertical oscillations of the balloon and the displacements of the isentropic surfaces are expected to be nonsynchronous because  $\omega_B$  does not correspond to any atmospheric frequency ( $\omega_B > N$ ), we assume that the covariance  $E[\delta z_B \times \delta \zeta_\theta]$  is negligible compared with the variance of  $\delta z_B$ , i.e.,

$$\text{Cov}(\delta\theta, \delta z_B) = E[\bar{\theta}_z \delta z_B \times \delta z_B]. \tag{9}$$

Notice that, under the above hypothesis, the covariance of a nonconservative measured quantity  $X(T, u, v)$  reads as follows:

$$\text{Cov}(\delta X, \delta z_B) = E[\bar{X}_z \delta z_B \times \delta z_B]. \tag{10}$$

If  $\bar{\theta}_z$  is positive in the time interval during which the covariance is estimated,  $\text{Cov}(\delta\theta, \delta z_B)$  is expected to be positive. Moreover, if  $\bar{\theta}_z$  is strictly constant during the time interval,

$$\bar{\theta}_z = \frac{\text{Cov}(\delta\theta, \delta z_B)}{\text{Var}[\delta z_B]}. \tag{11}$$

If  $\bar{\theta}_z$  is not strictly constant, as is very likely the case, the  $\text{Cov}(\delta\theta, \delta z_B)/\text{Var}[\delta z_B]$  ratio can be interpreted as an estimate of the mean gradient  $\langle \bar{\theta}_z \rangle$  during the considered time interval at the flight level of the SPB. For a nonconservative quantities  $X$ ,

$$\bar{X}_z = \frac{\text{Cov}(\delta X, \delta z_B)}{\text{Var}[\delta z_B]}. \tag{12}$$

In the ideal case where  $\bar{\theta}_z$  is constant and there is no instrumental noise,  $\sigma_{\delta\theta} = \bar{\theta}_z \sigma_{\delta z_B}$  and the correlation coefficient  $r_P(\delta\theta, \delta z_B) = 1$ , for all  $\bar{\theta}_z > 0$ . This conclusion also holds

for the Spearman correlation  $r_S$  if a linear relation is assumed between  $\delta\theta$  and  $\delta z_B$ . If  $\bar{\theta}_z > 0$  but is no longer constant during the considered time interval, the correlation coefficient is smaller than 1 but is still positive, as the product  $\delta\theta \times \delta z_B$  is always positive. The correlation is further reduced, although remains positive, in the presence of uncorrelated noise (see Appendix B).

The first method to detect turbulent mixing is to check for a nonpositive correlation, i.e., a null or negative correlation, between  $\delta\theta$  and  $\delta z_B$ . In order to infer if the null hypothesis  $H_0$  has to be rejected – that is, if a positive correlation exists – a standard hypothesis test is performed. A confidence interval for the correlation coefficient is based on a Fisher transformation of the correlation estimate (Hotelling, 1953). Here, the  $H_0$  hypothesis is rejected if the correlation estimate exceeds half of its standard deviation (unilateral test), with the corresponding confidence level being 69.15 %. If the  $H_0$  hypothesis cannot be rejected, turbulent mixing is diagnosed, and the turbulence flag is set to “true”. Two turbulence indexes are built, either from the Pearson or Spearman correlations.

Figure 7 illustrates the time series (Fig. 7a) and histograms (Fig. 7b) of  $r_P$  and  $r_S$  during 1 week of flight 02\_STR2. Both correlations are estimated over time segments of 1 h. The light blue shaded areas show the  $\pm 1$  standard deviation interval for the Pearson correlations only. The thick green lines at the top of Fig. 7a display the time interval during which turbulence is detected, i.e., when the turbulence indexes are set to true.

As expected, the correlation coefficients are found to be positive most of the time. On a few occurrences during the time period shown in Fig. 7, turbulence is detected as the correlation coefficients approach zero. A good agreement in the time periods identified as turbulent is found regardless of the correlation method used.

### 3.2.3 The impact of instrumental noise on the correlation coefficients

The impact of measurement noise can be evaluated using the averages of the largest correlation coefficients, all corresponding to  $\bar{\theta}_z > 0$  a priori. The reader should recall that, without instrumental noise, the correlation  $(\delta\theta, \delta z_B)$  is ideally 1 if  $\bar{\theta}_z > 0$  and remains constant over 1 h. As shown by Eq. (B1) in Appendix B, it is the ratio of the instrumental noise to the variance of the “geophysical” signal that appears in the correlation coefficient. In other words, the larger the amplitude of the balloon oscillations about their EDS, the less the measurement noise reduces the correlation coefficient.

The Spearman and Pearson correlation coefficients have been estimated for both potential temperature increments,  $\delta\theta_C$  and  $\delta\theta_S$ , and for both altitude increments,  $\delta z_P = -\delta P/\rho_C$  and  $\delta z_{GPS}$ . Thus, four turbulence indexes coefficients are estimated. We have then averaged the 50 % of cor-

Strateole-2.0 flt02 STR2 2019-12-08T00:00 – 2019-12-14T23:59

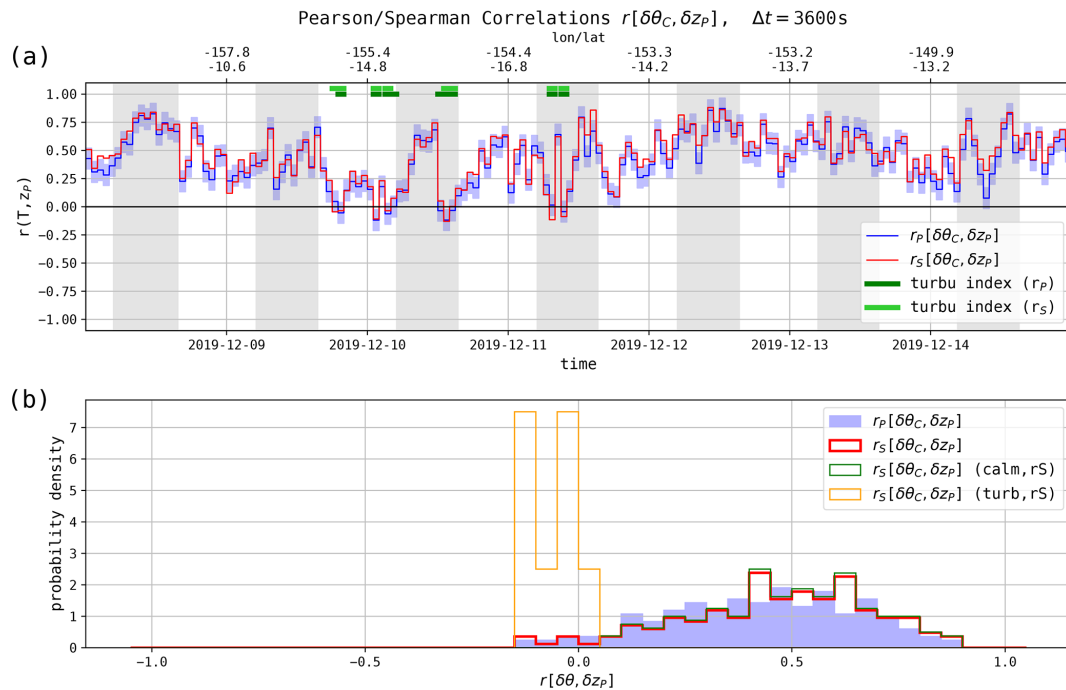


**Figure 7.** (a) Time series of correlation coefficients  $r_P$  and  $r_S$  applied to the increments' potential temperature derived from  $T_C$  and vertical displacements from  $z_P$ . The correlations are evaluated on 1 h time segments (120 samples). The time series runs for 7 d, from 8 to 15 December 2019. The gray vertical stripes indicate nighttime. The light blue shaded areas show the  $\pm 1$  standard deviation interval for the Pearson correlations. (b) Histograms of the two correlation coefficients obtained during the week. The blue shading and thick red line correspond to all of the 1 h time segments, and the thin green and orange lines correspond to the calm (nonturbulent) and turbulent time intervals, respectively.

relation coefficients with the largest values, i.e., the quantiles 50–100 of the coefficients, for each of the eight flights (Table 4). These averaged coefficients give information, at least relatively, on the quality of the data and on the performance of the turbulence estimators: the larger the correlations, the smaller the impact of instrumental noise.

Table 4 again illustrates that flight 03\_TTL3 is abnormally noisy because of the poorer (potential) temperature measurements (see Table 2). Systematically, we observe the following:

1. the correlations are larger when using  $\theta_C$  rather than  $\theta_S$ ,
2. there is a slight amelioration in using  $\delta z_P$  rather than  $\delta z_{GPS}$ ,
3. the Spearman correlations ( $r_S$ ) are slightly larger than the Pearson correlations ( $r_P$ ).

We shall, therefore, prefer the Spearman estimator, using  $\delta T_C$  (and derived  $\delta\theta_C$ ) combined with  $\delta z_P$ , in evaluating both the correlations and the vertical gradients from which the turbulent indexes are estimated, as the impact of instrumental noise appears to be lower in this estimator.

### 3.2.4 The Richardson method

The second detection method is based on an evaluation of the local Richardson number ( $Ri$ ). Notice that  $\bar{\theta}_z$  (Eq. 11) is the slope of a least squares linear regression between the 120 potential temperature increments ( $\delta\theta$ ) and vertical displacement increments ( $\delta z_B$ ). This method of estimating the vertical gradient of the potential temperature is labeled the least squares fitting (LSF) method in the following. An alternative fitting method, the so-called Theil–Sen fitting (TSF) method, has also been used (Sen, 1968). The Theil–Sen estimator is defined as the median of the slopes of all lines through pair of points of the sample. It is a nonparametric and robust method that is almost insensitive to outliers. Both fitting methods have been applied to estimate the vertical gradients of several measured quantities, such as  $T$  and  $P$  or the horizontal wind velocities  $u$  and  $v$  (Eq. 12).

Two estimates of the mean Brunt–Väisälä frequency are thus computed with either the LSF or the TSF, applied to  $\delta T_C$  and  $\delta z_P$ , which were identified as the less noisy estimates of the air temperature and vertical displacements, respectively (see Tables 2 and 3). The squared shear, evaluated

**Table 4.** Averages of the 50 % of correlation coefficients with the largest values between  $\delta\theta$  and  $\delta z$ . The Spearman and Pearson coefficients are displayed for the four combinations between  $\delta\theta_S$  or  $\delta\theta_C$  and  $\delta z_P$  or  $\delta z_{GPS}$ . About 1200 coefficients are averaged here for each flight. The largest correlation coefficient is displayed in bold for each flight. The larger the correlations, the smaller the impact of instrumental noise (see text).

Flight ID	$r_S$	$r_P$	$r_S$	$r_P$	$r_S$	$r_P$	$r_S$	$r_P$
	$\delta\theta_S, \delta z_P$	$\delta\theta_S, \delta z_P$	$\delta\theta_S, \delta z_{GPS}$	$\delta\theta_S, \delta z_{GPS}$	$\delta\theta_C, \delta z_P$	$\delta\theta_C, \delta z_P$	$\delta\theta_C, \delta z_{GPS}$	$\delta\theta_C, \delta z_{GPS}$
01_STR1	0.563	0.566	0.544	0.540	<b>0.592</b>	0.589	0.570	0.561
02_STR2	0.640	0.638	0.643	0.640	0.681	0.671	<b>0.683</b>	0.673
03_TTL3	0.402	0.284	0.392	0.278	<b>0.464</b>	0.319	0.457	0.315
04_TTL1	0.614	0.604	0.603	0.588	<b>0.678</b>	0.646	0.665	0.630
05_TTL2	0.605	0.572	0.600	0.566	<b>0.668</b>	0.657	0.661	0.648
06_STR1	0.569	0.549	0.547	0.524	<b>0.622</b>	0.593	0.603	0.569
07_STR2	0.585	0.566	0.563	0.537	<b>0.587</b>	0.556	0.564	0.527
08_STR2	0.639	0.631	0.638	0.629	<b>0.699</b>	0.685	0.697	0.683

from the vertical gradients of the horizontal velocities, is obtained similarly. Hence, two turbulence indexes are built using LSF and TSF estimates of the Richardson number and are set to true if  $Ri \leq 1/4$ .

Figure 8a displays the vertical gradients of temperature for the same 1-week time series as that shown in Fig. 7. Estimates are shown for only the thermocouple temperatures and vertical displacements obtained with the pressure increments. Time series (not shown) obtained from other pairs of variables (using  $T_S$  or  $T_C$  or using  $z_{GPS}$  or  $z_P$ ) are very similar to the one presented, regardless of the fitting method used. The uncertainty ( $\pm 1$  standard deviation) is shown in light red for the LSF estimator. The turbulence detection criteria based on the Richardson number are also displayed (thick green lines at the top of the figure). Figure 8b shows the probability distribution functions (PDFs) of the vertical gradients of temperature shown above (blue shading and thick curve). PDFs corresponding to turbulent and calm (i.e., nonturbulent) periods according to the Richardson number criterion are also displayed using thin lines.

First, it should be noticed that the choice of the LSF or TSF estimates for the vertical gradient of temperature or for the turbulence index has only a minor impact. Similarly, the choice of parameters ( $z_P$  or  $z_{GPS}$ ,  $T_C$  or  $T_S$ ) and any combination of those has little influence on the detection of turbulence layers (not shown). Figure 8 also clearly illustrates that the time periods flagged as turbulent by the Richardson number index are associated with the small-value tail of the temperature gradient PDF ( $dT/dz \lesssim -10 \text{ K km}^{-1}$ ). Finally, those time periods are essentially the same as the one shown in Fig. 7, obtained using the correlation method.

## 4 Results

### 4.1 Turbulence detection with the correlation method

Figure 9a displays the time series of both the Spearman and Pearson correlation coefficients between  $\delta\theta_C$  and  $\delta z_P$  for the

whole flight 02\_STR2. As done previously, the correlations are estimated on time segments of 1 h (120 samples). They range from  $\sim -0.5$  to 0.96. Both time series exhibit very similar variations, showing time intervals lasting several days with relatively large correlations ( $> 0.7$ ) and short bursts of time with low or even negative correlations. Two turbulence indexes inferred from the Spearman and Pearson correlation methods are shown as thick green lines at the top of Fig. 9a. The fraction of time during which the flow is detected as turbulent for flight 02\_STR2 is 4.5 % (4.4 %) from the Spearman (Pearson) correlations (see Table 5). Time series and histograms of correlations obtained using measurements of  $\delta\theta_S$  or  $\delta z_{GPS}$  (not shown) provide time series that are almost indistinguishable from those shown in Fig. 9.

Figure 9b shows the PDFs of the two correlation coefficients over the whole flight (blue shading and thick red line). Both distributions are observed to be almost identical, although  $r_S$  is slightly and systematically larger than  $r_P$  for correlations larger than 0.5. The average values for both correlation coefficients are close:  $\overline{r_S[\delta\theta_C, \delta z_P]} = 0.50$  and  $\overline{r_P[\delta\theta_C, \delta z_P]} = 0.48$ . The thin lines show the PDFs of  $r_S$  for solely turbulent (orange) and solely laminar time periods (green). The PDFs associated with the laminar time periods are almost identical to those of the whole flight, as they correspond to about 95 % of the data. The turbulent time periods correspond only to the small-value tail of the overall distribution.

The fractions of time during which the flow is found to be turbulent using the correlation method are reported in Table 5 for the eight flights of the campaign. Overall, they look very consistent, typically ranging between 4.5 % and 6.5 %, with the exception of flight 03\_TTL3, which is associated with noisier temperature measurements.

Strateole-2.0 flt02 STR2 2019-12-08T00:00 - 2019-12-14T23:59

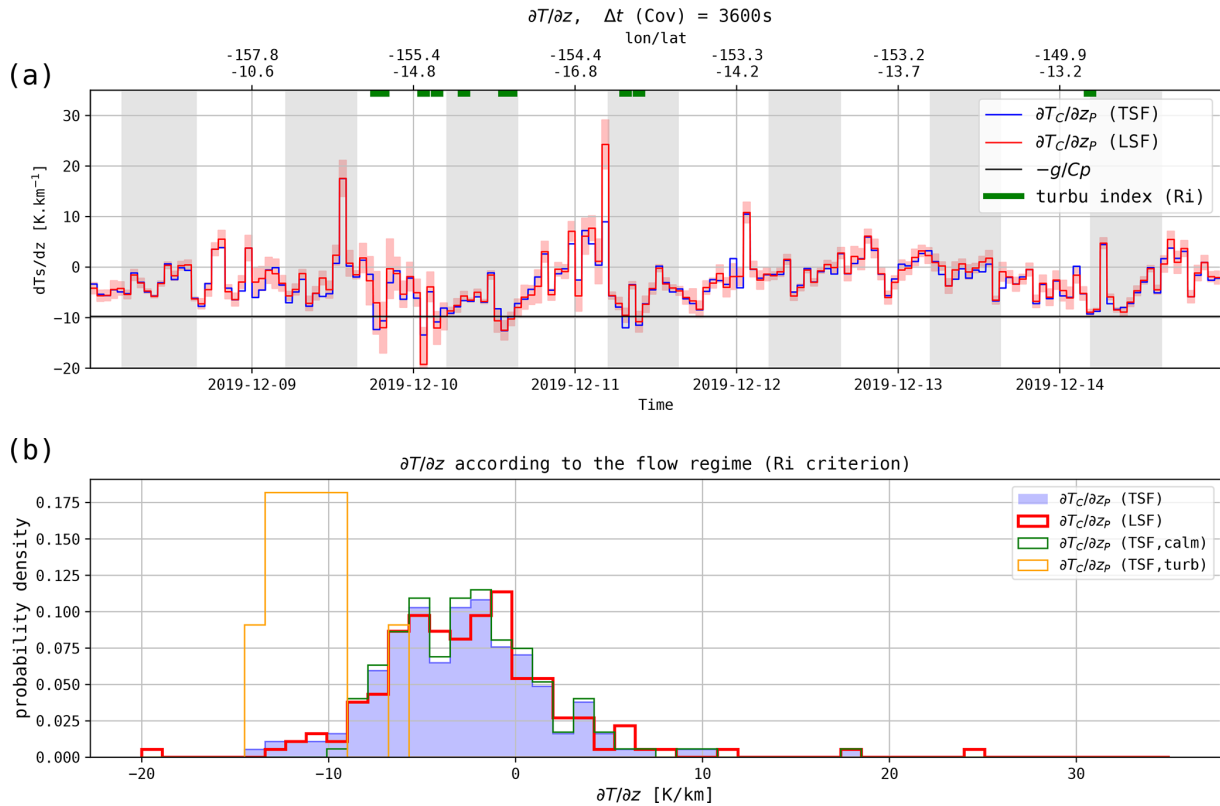


**Figure 8.** (a) Time series of  $\partial T/\partial z$  estimated by two respective fitting methods, least squares fitting (LSF) and Theil–Sen fitting (TSF), from  $T_C$  and  $z_p$ . Linear fits are performed on 1 h time segments (120 samples). The light red shaded areas show the  $\pm 1$  standard deviation interval for the LSF estimates. (b) Histograms of the temperature gradients from the two respective methods. The histograms corresponding to the turbulent and laminar time segments are also plotted (light curves).

**Table 5.** Fraction of time (percent) during which the flow is found to be turbulent. Turbulence is diagnosed from the correlation method based of  $\delta\theta_C$  and  $\delta z_p$  (second and third columns) and from the  $Ri(\delta\theta_C, \delta z_p)$  criterion (last column).

Flight ID	$r_S(\delta\theta_C, \delta z_p)$	$r_P(\delta\theta_C, \delta z_p)$	$Ri(\delta\theta_C, \delta z_p)$
01_STR1	5.1	4.9	3.7
02_STR2	4.5	4.4	3.7
03_TTL3	11.2	21.5	15.6
04_TTL1	3.8	4.9	3.4
05_TTL2	6.6	6.6	5.7
06_STR1	5.8	6.6	4.3
07_STR2	5.5	6.3	3.3
08_STR2	5.5	6.2	5.7

**4.2 Estimations of the vertical temperature gradient with the fitting methods**

Figure 10 shows estimates of  $\partial T/\partial z$  for flight 02\_STR2 inferred from linear fitting of the increments of temperature

and vertical displacements during hourly intervals. More precisely, Fig. 10a shows the vertical temperature gradient obtained with the TSF method applied to  $\delta T_C$  and  $\delta z_p$ . Time series obtained using other combinations of measured variables and fitting methods (not shown) are almost indistinguishable from the one shown in Fig. 10. The dry adiabatic lapse rate  $\Gamma = -g/c_p$  is also indicated as a black line. The turbulence index based on  $Ri$  is shown as a thick green discontinuous line at the top of Fig. 10a. Figure 10b shows the PDFs of  $\partial T/\partial z$  for the whole flight and for the respective calm and turbulent time periods. The distribution of  $\partial T/\partial z$  is found to be very asymmetric, with the mode being close to  $-4 \text{ K km}^{-1}$ . Most of the turbulent cases are associated with  $\partial T/\partial z < \Gamma$ , with a few of them being associated with  $\partial T/\partial z > \Gamma$ . The cumulative distribution functions (CDFs) of the temperature gradients are displayed in Fig. 10c. About 80 % of the detected turbulent cases, associated with  $Ri < 0.25$ , correspond to a super-adiabatic temperature gradient.

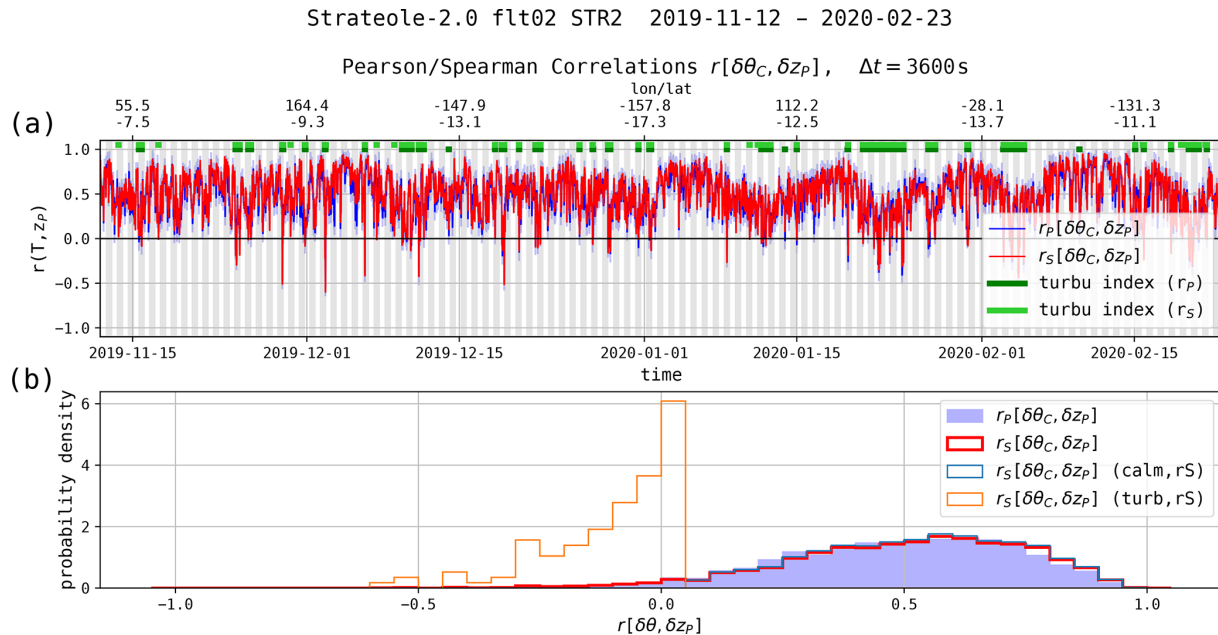


**Figure 9.** (a) Time series of the Spearman and Pearson correlation coefficients between  $\delta\theta_C$  and  $\delta z_P$  during flight 02\_STR2 (103 d). The turbulence indexes deduced from the two correlations are shown (thick green lines at the top of the plot). (b) Histograms of the Spearman (thick line) and Pearson (filled) coefficients for flight 02\_STR2. Also shown are the histograms corresponding to the turbulent and laminar cases (thin lines). The time series and histograms of the two correlation coefficients are very similar, even though a few differences in turbulence detection are visible.

Based on  $\partial T/\partial z$  estimates, the Brunt–Väisälä and NBO frequencies can be evaluated, see Eqs. (1) and (2). Figure 11 displays the squared Brunt–Väisälä ( $N^2$ ), the theoretical NBO ( $\omega_{\text{NBO}}^2$ ), and the observed balloon ( $\omega_{\text{B}}^2$ ) frequencies for the whole 02\_STR2 flight. The Brunt–Väisälä and NBO frequencies are deduced from the hourly estimates of  $\partial T/\partial z$ . The observed balloon frequencies are directly estimated from observations of the balloon oscillations (Fig. 3). A 60 min running average is then applied to the raw  $\omega_{\text{B}}$  time series. The three frequencies are close to but distinct from one another, with the observed balloon frequency ranging between  $N$  and  $\omega_{\text{NBO}}$ . The CDF of frequency ratios (Fig. 11c) reveals that  $\sim 95\%$  of the measured  $\omega_{\text{B}}$  are smaller than the  $\omega_{\text{NBO}}$  estimates and that 19% of  $\omega_{\text{B}}$  are smaller than  $N$ . This property is consistent with numerical simulations of the motion of a spherical SPB assuming that atmospheric forcing occurs at frequencies lower than the Brunt–Väisälä frequency (Podglajen et al., 2016, in particular see their Supplement).

Figure 12 shows the histograms of  $T_z = \partial T_C/\partial z_P$  for flight 3 obtained from the TSEN measurements (TSF method) and from the RACHuTS temperature profiles – down to 2 km below the balloon. The vertical gradients of the RACHuTS temperature are estimated using 30 m vertical segments. The RACHuTS histogram has common features with the TSEN histograms: an asymmetric distribution, the same negative modes, and a sharp transition around  $-10^\circ\text{C km}^{-1}$ . These distributions are considered to be con-

sistent, despite the fact that they are not obtained in the same altitude domain nor simultaneously.

### 4.3 Turbulence detection with the $Ri$ method

Figure 13 shows estimates of the Richardson number along flight 02\_STR2, obtained using either the LSF or TSF estimates, with  $T_C$ ,  $z_P$ ,  $u$ , and  $v$  observations. The corresponding two turbulence indexes ( $Ri \leq 1/4$ ) are also shown in Fig. 13a (green thick line). Figure 13b displays the histograms of the two  $Ri$  estimates. The time series and histograms of the two  $Ri$  estimates look very similar, even though a few differences in the turbulence detection are visible.

As shown in Table 5, the fraction of time during which the flow is found to be turbulent according to the  $Ri$  criterion is 3.7% for flight 02\_STR2. More generally, the detection of turbulent flow during the Strateole-2 C0 campaign ranges from 3.3% to 5.7% of the time, with the exception of flight 03\_TTL3.

## 5 Discussion

### 5.1 Possible impact of wake on the temperature measurements

Due to the vertical oscillations of the balloon, the  $T$  sensors were possibly in the wake of the balloon or of the flight chain. Note that we expect the balloon wake to be warm during



Strateole-2.0 flt02 STR2 2019-11-12 - 2020-02-23

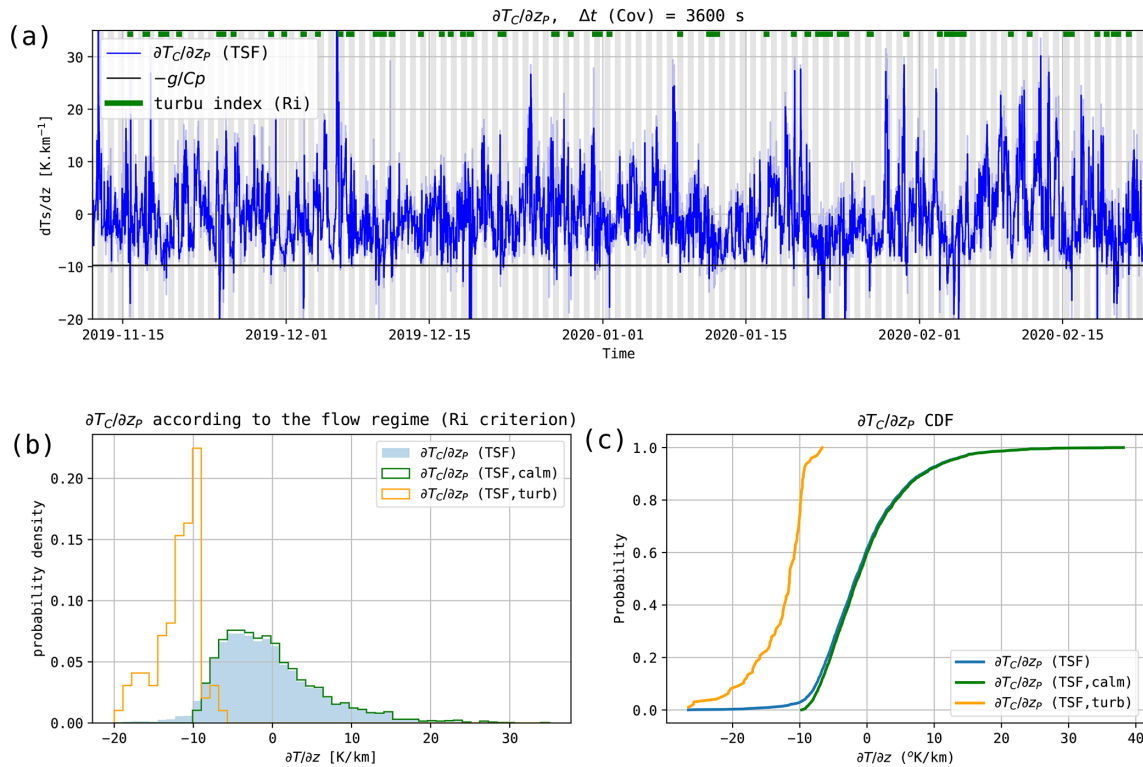


**Figure 10.** (a) Two estimates of  $\partial T_C/\partial z_P$  for flight 02\_STR2, from the linear fitting of  $T_C$  and  $\delta z_P$  at hourly intervals. The black line shows the adiabatic lapse rate  $-g/c_p$ . The  $Ri$  turbulence index is drawn on the top of the figure as a thick green discontinuous line. (b) Histograms of  $\partial T_C/\partial z_P$  for all of the time intervals (blue shading) and for the respective laminar and turbulent cases (thin lines). (c) CDFs of the temperature gradients.

daytime and cold during nighttime, with the balloons being cooler than the ambient air during nighttime.

The temperature sensors were located 27 m below the balloon base (except for during the 03\_TTL3 flight) and 15 m below the EUROS gondola. The diameter of the balloons was either 11 m (TTL) or 13 m (STR). On all but the TTL3 flights, the  $T$  sensors were located 7 m below the last gondola in the flight chain. Flight 03\_TTL3, carrying the RACHuTS system, is an exception, as the temperature sensors were located 30 cm from the EUROS gondola.

The question of the possible impact of the wake on temperature measurements has been taken into account. Indeed, we have calculated the statistics, vertical gradients, and correlations, considering only the downward phases of the oscillations, i.e., when the temperature sensors (which are located at the lower end of the flight chain) sample “fresh” air if a minimum shear exists. The resulting time series (not shown) are noisier because we only consider about half of the samples. However, both time series of correlations and temperature gradients have similar characteristics to those calculated when considering all samples, showing the same succession of stable and unstable periods. Therefore, we conclude that

the impact of the wake does not significantly affect the estimated statistics, correlations, nor covariances, and, due to the increase in noise, we choose to consider all of the samples.

## 5.2 Comparison of the turbulence indexes

Table 6 shows the percentage of identical detections (laminar or turbulent) of the four turbulence indexes ( $r_P$ ,  $r_S$ ,  $Ri_{LSF}$ , and  $Ri_{TSF}$ ) for the eight balloon flights. The percentage of similar detections ranges from 97.9 % ( $r_S$  vs.  $Ri_{LSF}$ ) to 99.07 %. However, as pointed out by an anonymous reviewer, such overall agreement does not imply equally good agreement between estimators when turbulence is detected. Choosing  $Ri_{TSF}$  as a reference, we compared the diagnoses with the other three estimators ( $Ri_{LSF}$ ,  $r_P$ , and  $r_S$ ). Figure 14 shows the percentages of similar and different detections when the flow is diagnosed as turbulent (T) or laminar (L). It reveals that the detections are similar for more than 99 % of cases if the flow is diagnosed as laminar. If the flow is diagnosed as turbulent, the rate of identical detections drops to about 80 %, with the comparison being the worst for  $r_P$  (76 %) and comparable for  $r_S$  and  $Ri_{LSF}$  (83.2 % and 85.4 %, respectively). We believe that these differences mainly result

Strateole-2.0 flt02 STR2 2019-11-12 - 2020-02-23

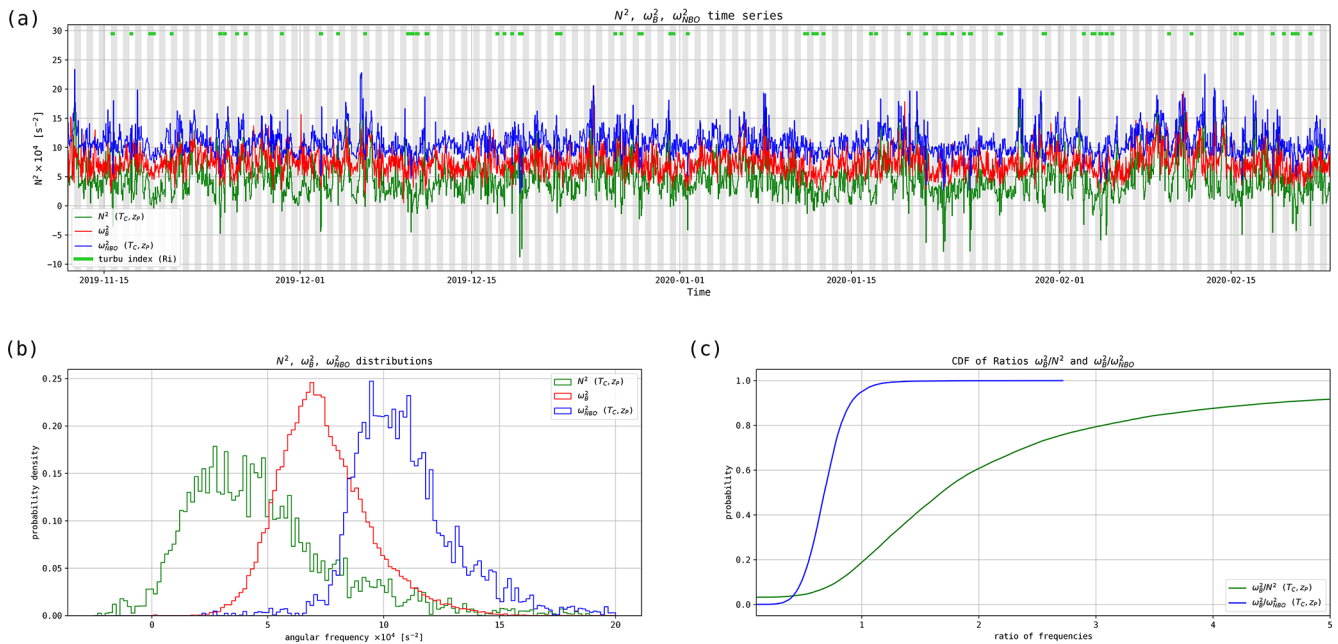


**Figure 11.** Times series (a) and histograms (b) of the Brunt–Väisälä, NBO, and observed balloon frequencies. The Brunt–Väisälä and NBO frequencies are deduced from the estimates of  $\partial T/\partial z$  from  $\text{Cov}(\delta T_C, \delta z_P)$ . (c) CDF of the  $\omega_B^2/N^2$  and  $\omega_B^2/\omega_{BBO}^2$  ratios.

Strateole-2.0 flt03 TTL3 2019-11-19 - 2020-02-28  
 $\partial T_C/\partial z_P$ ,  $\Delta t$  (Cov) = 3600s

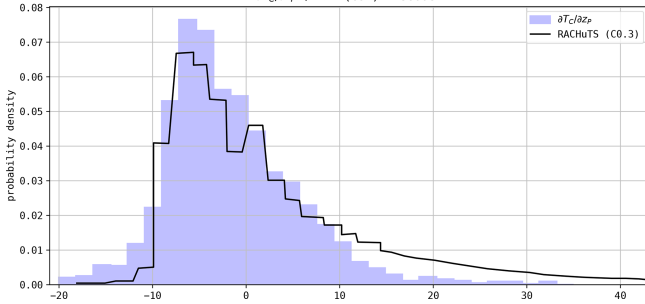


**Figure 12.** Histograms of  $\partial T/\partial z_P$  from the covariance of the TSEN measurements (blue shading) and from the RACHuTS temperature profile (black line). The two histograms have common characteristics, despite the fact that they are not obtained at the same altitude levels.

from the fact that the threshold values, zero correlation or  $Ri = 0.25$ , correspond to the tails of the distributions of these estimates (see the histograms in Figs. 9 and 13). When the atmosphere is weakly stratified, threshold effects are likely to be important, leading to some differences in the diagnoses of flow conditions.

We also found that the time fraction of turbulent episodes obtained by the  $Ri$  criterion is almost always smaller than that obtained by the correlation methods (Table 5). This can be partly due to the threshold values of the hypothesis tests of a null correlation (i.e., to the choice of a confidence interval).

### 5.3 Occurrences of negative values for $Ri$ and $N^2$

The time series of  $N^2$  (Fig. 11) and  $Ri$  (Fig. 13) show some negative values. For the considered flight (02\_STR2), the occurrence frequency of negative  $N^2$  is 3.4 % (from the Theil–Sen regression performed on  $T_C$  and  $z_P$ ). Such a negative  $Ri$  ( $N^2$ ) can result from both the dispersion of the temperature gradient estimates and the occurrence of episodes of unstable stratification.

Negative estimates of  $N^2$  (or  $Ri$ ) could be due to the precision of the temperature gradient estimates, which are expected to be scattered around a value close to  $-10^\circ\text{C km}^{-1}$  in the case of neutral stratification. Temperature gradients are estimated from the covariance of temperature increments and displacements, with these covariances scattered around their mean values. As a result,  $N^2$  estimates can be negative even if the stratification is neutral or nearly neutral.

However, unstable stratifications ( $N^2 < 0$ ) seem to occur in the lower stratosphere, as they have been reported in the literature. For instance, the detection of turbulence by the Thorpe method from in situ measurements is based on observations of  $\partial\theta/\partial z < 0$ , i.e.,  $N^2 < 0$  (Thorpe, 1977). The probability of occurrence of such unstable layers likely depends on the vertical resolution of the profiles (e.g., Wilson et al., 2011) but is not zero. In the lower stratosphere, KHIs are expected to be the main source of instability. For KHIs, turbulence is expected to be triggered for  $0 < Ri < 1/4$ , i.e., for  $N^2 > 0$ ; however, once it is developed, the stratification can

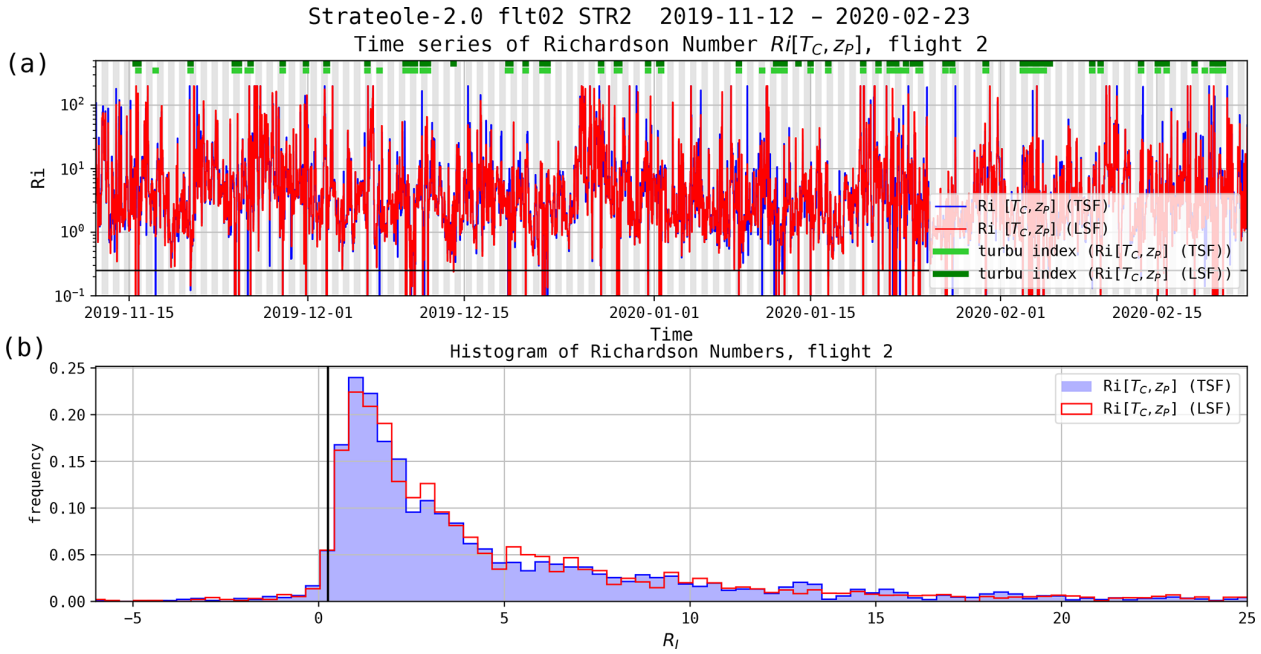


**Figure 13.** (a) Richardson number estimates from  $T_C$ ,  $u$ ,  $v$ , and  $z_P$  using the respective least squares fitting (LSF) and Theil–Sen fitting (TSF) methods. The thick black line shows the threshold  $Ri = 0.25$ . The two inferred turbulence indexes are shown (thick green lines at the top of the plot). (b) Histograms of the two Richardson number estimates.

**Table 6.** Percentage of identical turbulence detections from four turbulence index using  $(T_C, z_P)$  for flight 02\_STR2.

	$r_P[T_C, z_P]$	$r_S[T_C, z_P]$	$Ri_{LSF}[T_C, z_P]$	$Ri_{TSF}[T_C, z_P]$
$r_P[T_C, z_P]$	100	98.95	98.46	98.42
$r_S[T_C, z_P]$		100	97.90	98.59
$Ri_{LSF}[T_C, z_P]$			100	99.07

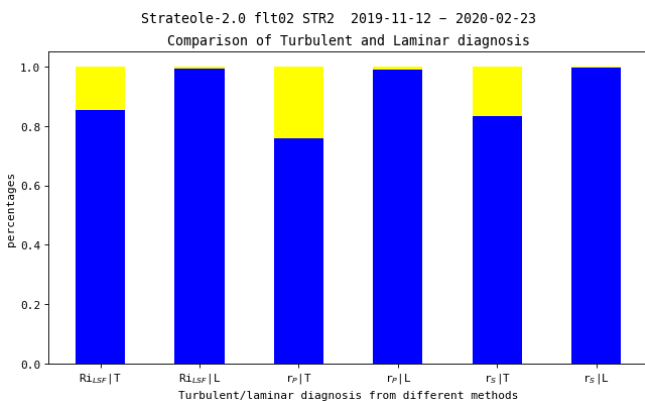


**Figure 14.** Percentages of true (similar) and false (different) detections for turbulent (T) and laminar (L) episodes diagnosed by the  $Ri_{TSF}$  criterion. The three estimators,  $Ri_{LSF}$ ,  $r_P$ , and  $r_S$ , are compared to  $Ri_{TSF}$ . The rate of agreement is larger than 99 % in the case of laminar flow and about 80 % in the case of turbulent flow.

become almost neutral ( $N^2 \approx 0$ ) or even unstable ( $N^2 < 0$ ) as a result of stirring and mixing. Therefore, it is plausible that the occurrence of unstable episodes may also contribute to negative values of  $N^2$  or  $Ri$  estimated from covariances.

Numerical simulations indicate that large temperature gradients are expected at the edges of turbulent layers (Fritts et al., 2003; Werne and Fritts, 1999). These strong temperature gradients are also commonly observed from radiosonde profiles when turbulence detection is performed by the Thorpe method (e.g., Luce et al., 2002). It is clear that sampling by balloons drifting within an air mass, and not cutting vertically through it as done by a radiosonde, will not allow one to identify turbulence from these sharp temperature gradients at the layer edges. Only the central part of the turbulent region, in which stratification is almost zero, can be identified as turbulent.

### 5.4 Spatial inhomogeneity of turbulence detections

The detection of turbulent episodes is far from uniform around the globe. Figure 15 shows the positions of turbu-

lence detections (green dots) for the eight flights of the C0 campaign. Turbulence detections seem to be very rare over some regions (e.g., the southern Atlantic Ocean) and quite frequent over other regions (e.g., the Maritime Continent or the western Pacific). At the present stage, this result is only qualitative; however, interestingly, these inhomogeneities are likely related to the causes of the turbulence occurrences (see for instance Fritts and Alexander, 2003). A study examining processes that cause turbulence in the UTLS is in progress.

## 6 Summary and concluding remarks

The present paper dealt with the detection of turbulence on superpressure balloon flights that drift for several months in the UTLS. During the Strateole-2 C0 campaign, eight SPBs were launched. Statistical methods to infer the flow regime, either laminar or turbulent, in which the SPBs were drifting are described. Some properties of the local stratification of the flow are also inferred. These methods are based on in situ GPS altitude, pressure, and temperature measurements, which were performed on all of the SPBs of the Strateole-2 C0 campaign with a time resolution of 30 s.

We make use of the SPB oscillations about their equilibrium density surface, which typically enable SPBs to vertically explore the atmosphere over 30 m (peak-to-peak displacements). The observed periods of oscillation,  $\sim 220$  s on average, are significantly smaller than the Brunt–Väisälä period. The large amplitude of these balloon motions at frequencies higher than the Brunt–Väisälä frequency (where turbulence is expected to occur) makes it very difficult, if not impossible, to detect turbulence from the direct characterization (i.e., from the variance or power spectra) of high-frequency fluctuations. On an other hand, thanks to the vertical motions of the SPBs around their EDS, the vertical gradients of any measured quantity can be estimated, either via the covariance between the increments of this quantity and those of the vertical displacements or, equivalently, via the linear fit between these two increments. For the present study, covariances and linear fits have been estimated on data segments of 1 h, i.e., 120 data samples.

Several turbulence indexes (true or false) are defined and compared. A first index is based on an inference test on the correlation between potential temperature and altitude increments. A null correlation is expected in the case of turbulent mixing, as the vertical gradient of potential temperature tends to zero. Two correlation coefficients, the Pearson and Spearman coefficients, have been tested and compared for the eight balloon flights. Alternatively, based on a linear fit between increments, vertical temperature gradients and horizontal wind can be evaluated at 1 h intervals, from which the local Richardson number can be deduced. A second turbulence index is then based on the criterion  $Ri < 0.25$ . These different turbulence indexes compare well, as they coincide for more than 97 % of cases.

SPBs sample the atmosphere without any spatial or temporal sampling bias, drifting nights and days, over oceans and continents, and above convective and non-convective regions. The fraction of time during which the flow is found to be turbulent in the lower stratosphere appears to be quite small, ranging from 3.3 % to 6.6 %. Because of the lack of sampling bias, such a fraction of time can be interpreted as a fraction of space. The probability of occurrence of instabilities is far from being uniform in time (or space). Periods of several days are frequently observed during which the atmosphere is stable, i.e., without any instability. On the other hand, during certain periods, the frequency of instabilities appears to be quite high. At first sight, these differences could be attributable to the underlying deep convection, as observed, for example, when the balloons are flying over the Maritime Continent. However, this remains a very preliminary conclusion that needs to be substantiated in future work.

## Appendix A: Estimation of the uncorrelated noise

The measured signal is assumed to contain an uncorrelated and centered noise contribution. This noise level is estimated on short data segments ( $\sim 20$  data samples), with the useful signal being described by a polynomial fit of degree  $n$ . The time series of quantity  $X$  reads

$$\underline{X}_i = X_i + \xi_i \quad (1 \leq i \leq n), \tag{A1}$$

where  $\underline{X}_i$  is the measured signal, and  $\xi_i$  is an uncorrelated noise of variance  $\sigma_\xi^2$ . The measured first increment reads

$$\delta \underline{X}_i = X_{i+1} - X_i + \xi_{i+1} - \xi_i. \tag{A2}$$

If  $X_i$  is constant, i.e.,  $X_{i+1} - X_i = 0$ , the variance of  $\delta \underline{X}_i$  reduces to

$$\text{Var}[\delta \underline{X}_i] = 2\text{Var}[\xi] = 2\sigma_\xi^2. \tag{A3}$$

The measured second increment reads

$$\begin{aligned} \delta^2 \underline{X}_i &= \delta \underline{X}_{i+1} - \delta \underline{X}_i \\ &= X_{i+2} - 2X_{i+1} + X_i + \xi_{i+2} - 2\xi_{i+1} + \xi_i. \end{aligned} \tag{A4}$$

If  $X_i$  varies according a linear trend, i.e.,  $X_{i+2} - 2X_{i+1} + X_i = 0$ , the variance of  $\delta^2 \underline{X}_i$  reduces to

$$\begin{aligned} \text{Var}[\delta^2 \underline{X}_i] &= \text{Var}[\xi] + 4\text{Var}[\xi] + \text{Var}[\xi] \\ &= \sum_{k=0}^2 \binom{2}{k}^2 \sigma_\xi^2 = 6\sigma_\xi^2. \end{aligned} \tag{A5}$$

The measured  $n$ th increment reads

$$\begin{aligned} \delta^n \underline{X}_i &= \delta^{n-1} \underline{X}_{i+1} - \delta^{n-1} \underline{X}_i = \sum_{k=0}^n (-1)^{n-k} \binom{n}{k} X_{i+k} \\ &\quad + \sum_{k=0}^n (-1)^{n-k} \binom{n}{k} \xi_{i+k}. \end{aligned} \tag{A6}$$

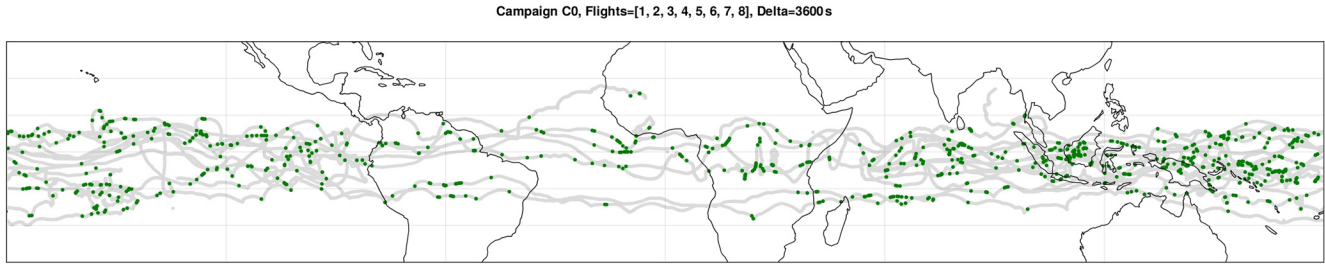


**Figure 15.** The positions of turbulent patches are shown as green dots for the eight flights of the C0 campaign. Each dot corresponds to a 1 h time interval. The detections are based on the  $Ri_{TSF}$  criterion. The detected turbulence episodes are far from uniform around the globe.

If  $X_i$  is described by a polynomial of degree  $n - 1$ , the first term on the right-hand side of Eq. (A6) cancels, and the variance of  $\delta^n X_i$  reduces to

$$\text{Var}[\delta^n X_i] = \sum_{k=0}^n \binom{n}{k}^2 \sigma_\xi^2. \tag{A7}$$

Increasing the order of differentiation enhances the relative contribution of the uncorrelated signal in the time series. After several differentiations, the variance of the differentiated time series is expected to converge to the weighted variance of the uncorrelated noise.

**Appendix B: Impact of instrumental noise on the correlation coefficients**

The Pearson or Spearman correlation coefficients ( $\rho_P$  and  $\rho_S$ , respectively) will be reduced because of uncorrelated noise in the time series of  $\delta z_B$  and  $\delta\theta$ . A simplistic model may help to illustrate this assertion. Let us note  $\underline{\theta}$ , the measured potential temperature, and  $\underline{z}_B$ , the measured altitude of the balloon. Assume that  $\underline{\theta}$  can be analyzed as  $\underline{\theta} = \theta + \eta$ , where  $\theta$  is the real value and  $\eta$  is a centered random noise. Similarly,  $\underline{z}_B = z_B + \zeta$ . The variance of the measured increments  $\delta X$  ( $X = \theta$  or  $z_B$ ) reads

$$\text{Var}[\delta X] = \text{Var}[\delta X] + 2\sigma_X^2,$$

where  $\sigma_X$  is the standard deviation of the random noise on  $X$ . Also,  $\text{Cov}[\delta \underline{\theta}, \delta \underline{z}_B] = \text{Cov}[\delta \theta, \delta z_B]$ . The expectation of the Pearson correlation coefficient  $\rho_P[\delta \underline{\theta}, \delta \underline{z}_B] = \text{Cov}[\delta \underline{\theta}, \delta \underline{z}_B] / (\text{Var}[\delta \underline{\theta}] \text{Var}[\delta \underline{z}_B])^{1/2}$  reads

$$\rho_P[\delta \underline{\theta}, \delta \underline{z}_B] = \frac{\rho_P[\delta \theta, \delta z_B]}{\left(1 + \frac{2\sigma_\eta^2}{\text{Var}[\delta z_B]} + \frac{2\sigma_\zeta^2}{\text{Var}[\delta \theta]} + \frac{4\sigma_\eta^2 \sigma_\zeta^2}{\text{Var}[\delta \theta] \text{Var}[\delta z_B]}\right)^{1/2}}, \tag{B1}$$

where  $\sigma_\theta^2$  and  $\sigma_\zeta^2$  are the variances of the noises on  $\theta$  and  $z_B$ , respectively. Thus, the correlation coefficients are expected to be significantly reduced due to the instrumental noise. However, they will retain the same sign as the correlation coefficients without instrumental noise.

*Data availability.* The balloon-borne TSEN and RACHuTS data used in this study were collected as part of Strateole-2, which is sponsored by CNES, CNRS/INSU, NSF, and ESA. The Strateole-2 data set is available at <https://doi.org/10.14768/7396b9ec-582f-4be2-8c37-c34ef41247a7> (Hertzog, 2021).

*Author contributions.* RW developed the data processing method and wrote the majority of the manuscript. CP participated in conditioning and processing the data. AP processed the RACHuTS data. AH is PI of Strateole-2 and preprocessed the raw data, making them available. AP and AH made important contributions with respect to extensive exchanges about the physics of superpressure balloon-borne measurements. All authors (RW, CP, AP, AH, MC, and RP) participated in numerous discussions to elaborate and improve the overall understanding of the physics of measurements, and all co-authors contributed significantly to writing the paper.

*Competing interests.* The contact author has declared that none of the authors has any competing interests.

*Disclaimer.* Publisher’s note: Copernicus Publications remains neutral with regard to jurisdictional claims in published maps and institutional affiliations.

*Acknowledgements.* The authors warmly thank the three reviewers for their thorough review of this article. Their remarks and suggestions have helped to improve the paper in a very significant way. The authors acknowledge support from the Agence Nationale de la Recherche (TuRTLES project). Clara Pitois is funded via a Sorbonne Université doctoral fellowship.

*Financial support.* This research has been supported by the Agence Nationale de la Recherche (grant no. ANR-21-CE01-0016-01) and the Centre National d’Études Spatiales (grant no. TOSCA).

*Review statement.* This paper was edited by Markus Rapp and reviewed by Ulrich Schumann and two anonymous referees.

## References

- Corcors, M., Hertzog, A., Plougonven, R., and Podglajen, A.: Observation of Gravity Waves at the Tropical Tropopause Using Superpressure Balloons, *J. Geophys. Res.-Atmos.*, 126, e2021JD035165, <https://doi.org/10.1029/2021JD035165>, 2021.
- Dörnbrack, A., Bechtold, P., and Schumann, U.: High-Resolution Aircraft Observations of Turbulence and Waves in the Free Atmosphere and Comparison With Global Model Predictions, *J. Geophys. Res.-Atmos.*, 127, e2022JD036654, <https://doi.org/10.1029/2022JD036654>, 2022.
- Ecklund, W. L., Gage, K. S., Nastrom, G. D., and Balsley, B. B.: A Preliminary Climatology of the Spectrum of Vertical Velocity Observed by Clear-Air Doppler Radar, *J. Appl. Meteorol. Clim.*, 25, 885–892, 1986.
- Fritts, D. C. and Alexander, M. J.: Gravity wave dynamics and effects in the middle atmosphere, *Rev. Geophys.*, 41, 1003, <https://doi.org/10.1029/2001RG000106>, 2003.
- Fritts, D. C., Bizon, C., Werne, J. A., and Meyer, C. K.: Layering accompanying turbulence generation due to shear instability and gravity-wave breaking, *J. Geophys. Res.*, 108, 8452, <https://doi.org/10.1029/2002JD002406>, 2003.
- Fueglistaler, S., Dessler, A. E., Dunkerton, T. J., Folkins, I., Fu, Q., and Mote, P. W.: Tropical tropopause layer, *Rev. Geophys.*, 47, RG1004, <https://doi.org/10.1029/2008RG000267>, 2009.
- Fujiwara, M., Yamamoto, M., Hashiguchi, H., Horinouchi, T., and Fukao, S.: Turbulence at the tropopause due to breaking Kelvin waves observed by the Equatorial Atmosphere Radar, *Geophys. Res. Lett.*, 30, 1171, <https://doi.org/10.1029/2002GL016278>, 2003.
- Haase, J., Alexander, M., Hertzog, A., Kalnajs, L., Davis, S., Ploufonven, R., Cocquerez, P., and Venel, S.: Around the world in 84 days, *EOS*, 99, <https://doi.org/10.1029/2018EO091907>, 2018.
- Hanna, S. R. and Hoecker, W. H.: The Response of Constant-Density Balloons to Sinusoidal Variations of Vertical Wind Speeds, *J. Appl. Meteorol. Clim.*, 10, 601–604, 1971.
- Hertzog, A.: STRATEOLE2 - C0: TSEN - Thermodynamics Sensor, LMD/IPSL [data set], <https://doi.org/10.14768/7396b9ec-582f-4be2-8c37-c34ef41247a7>, 2021.
- Hertzog, A. and Vial, F.: A study of the dynamics of the equatorial lower stratosphere by use of ultra-long-duration balloons 2. Gravity waves, *J. Geophys. Res.*, 106, 22745–22761, 2001.
- Hertzog, A., Alexander, M. J., and Plougonven, R.: On the Intermittency of Gravity Wave Momentum Flux in the Stratosphere, *J. Atmos. Sci.*, 69, 3433–3448, 2012.
- Hotelling, H.: New Light on the Correlation Coefficient and its Transforms, *J. Roy. Stat. Soc. B Met.*, 15, 193–225, 1953.
- Kalnajs, L. E., Davis, S. M., Goetz, J. D., Deshler, T., Khaykin, S., St. Clair, A., Hertzog, A., Bordereau, J., and Lykov, A.: A reel-down instrument system for profile measurements of water vapor, temperature, clouds, and aerosol beneath constant-altitude scientific balloons, *Atmos. Meas. Tech.*, 14, 2635–2648, <https://doi.org/10.5194/amt-14-2635-2021>, 2021.
- Luce, H., Fukao, S., Dalaudier, F., and Crochet, M.: Strong mixing events observed near the tropopause with the MU radar and high-resolution Balloon techniques, *J. Atmos. Sci.*, 59, 2885–2896, 2002.
- Luce, H., Wilson, R., Dalaudier, F., Nishi, N., Shibagaki, Y., and Nakajo, T.: Simultaneous observations of tropospheric turbulence from radiosondes using Thorpe analysis and the VHF MU radar, *Radio Sci.*, 49, 1106–1123, 2015.
- Mega, T., Yamamoto, M., Luce, H., Tabata, Y., Hashiguchi, H., Yamamoto, M., Yamanaka, M., and Fukao, S.: Turbulence generation by Kelvin-Helmholtz instability in the tropical tropopause layer observed with a 47 MHz range imaging radar, *J. Geophys. Res.*, 115, D18115, <https://doi.org/10.1029/2010JD013864>, 2010.
- Muhsin, M., Sunilkumar, S., Venkat Ratnam, M., Parameswaran, K., Krishna Murthy, B., Ramkuma, G., and Rajeev, K.: Diurnal variation of atmospheric stability and turbulence during different seasons in the troposphere and lower stratosphere derived from simultaneous radiosonde observations at two tropical stations in the Indian Peninsula, *Atmos. Res.*, 180, 12–23, 2016.
- Muhsin, M., Sunilkumar, S., Ratnam, M. V., Parameswaran, K., Mohankumar, K., Mahadevan, S., Murugadass, K., Muralaiah, P., Kumar, B. S., Nagendra, N., Emmanuel, M., Chandran, P., Koushik, N., Ramkumar, G., and Murthy, B.: “Contrasting features of tropospheric turbulence over the Indian peninsula”, *J. Atmos. Sol.-Terr. Phys.*, 197, 105179, <https://doi.org/10.1016/j.jastp.2019.105179>, 2020.
- Nastrom, G. D.: The response of superpressure balloons to gravity waves, *J. Appl. Meteorol.*, 19, 1013–1019, 1980.
- Podglajen, A., Hertzog, A., Plougonven, R., and Legras, B.: Lagrangian temperature and vertical velocity fluctuations due to gravity waves in the lower stratosphere, *Geophys. Res. Lett.*, 43, 3543–3553, 2016.
- Podglajen, A., Bui, T., Dean-Day, J., Pfister, L., Jensen, E., Alexander, M., Hertzog, A., Kärcher, B., Plougonven, R., and Randel, W.: Small-Scale Wind Fluctuations in the Tropical Tropopause Layer from Aircraft Measurements: Occurrence, Nature, and Impact on Vertical Mixing, *J. Atmos. Sci.*, 74, 3847–3869, <https://doi.org/10.1175/JAS-D-17-0010.1>, 2017.
- Satheesan, K. and Krishna Murthy, R.: Estimation of turbulence parameters in the lower atmosphere from MST radar observations, *Q. J. Roy. Meteor. Soc.*, 130, 1235–1249, 2004.
- Satheesan, K. and Murthy, R. F. K.: Turbulence parameters in the tropical troposphere and lower stratosphere, *J. Geophys. Res.*, 107, ACL 2-1–ACL 2-13, <https://doi.org/10.1029/2000JD000146>, 2002.
- Sen, P.: Estimates of the Regression Coefficient Based on Kendall’s Tau, *J. Am. Stat. Assoc.*, 63, 1379–1389, <https://doi.org/10.1080/01621459.1968.10480934>, 1968.
- Spearman, C.: The Proof and Measurement of Association between Two Things, *Am. J. Psychol.*, 15, 72–101, <https://doi.org/10.2307/1412159>, 1904.
- Sunilkumar, S., Muhsin, M., Parameswaran, K., Venkat Ratnam, M., Ramkumar, G., Rajeev, K., Krishna Murthy, B., Sambhu Namboodiri, K., Subrahmanyam, K., Kishore Kumar, K., and Shankar Das, S.: Characteristics of turbulence in the troposphere and lower stratosphere over the Indian Peninsula, *J. Atmos. Sol.-Terr. Phys.*, 133, 36–53, 2015.
- Thorpe, S. A.: Turbulence and mixing in a Scottish Lock, *Philos. T. Roy. Soc. A*, 286, 125–181, 1977.
- VanZandt, T. E., Nastrom, G. D., and Green, J. L.: Frequency spectra of vertical velocity from Flatland VHF radar data, *J. Geophys. Res.-Atmos.*, 96, 2845–2855, 1991.



- Vincent, R. A. and Hertzog, A.: The response of superpressure balloons to gravity wave motions, *Atmos. Meas. Tech.*, 7, 1043–1055, <https://doi.org/10.5194/amt-7-1043-2014>, 2014.
- Werne, J. and Fritts, D. C.: Stratified shear turbulence: Evolution and statistics, *Geophys. Res. Lett.*, 26, 439–442, <https://doi.org/10.1029/1999GL900022>, 1999.
- Wilson, R., Luce, H., Dalaudier, F., and Lefrère, J.: Turbulent Patch Identification in Potential Density/Temperature Profiles, *J. Atmos. Ocean. Tech.*, 26, 977–993, 2010.
- Wilson, R., Dalaudier, F., and Luce, H.: Can one detect small-scale turbulence from standard meteorological radiosondes?, *Atmos. Meas. Tech.*, 4, 795–804, <https://doi.org/10.5194/amt-4-795-2011>, 2011.
- Wilson, R., Luce, H., Hashiguchi, H., Shiotani, M., and Dalaudier, F.: On the effect of moisture on the detection of tropospheric turbulence from in situ measurements, *Atmos. Meas. Tech.*, 6, 697–702, <https://doi.org/10.5194/amt-6-697-2013>, 2013.
- Wilson, R., Hashiguchi, H., and Yabuki, Y.: Vertical Spectra of Temperature in the Free Troposphere at Meso-and-Small Scales According to the Flow Regime: Observations and Interpretation, *Atmosphere*, 9, 415, <https://doi.org/10.3390/atmos9110415>, 2018.
- Yamamoto, M. K., Fujiwara, M., Horinouchi, T., Hashiguchi, H., and Fukao, S.: Kelvin-Helmholtz instability around the tropical tropopause observed with the Equatorial Atmosphere Radar, *Geophys. Res. Lett.*, 30, 1476, <https://doi.org/10.1029/2002GL016685>, 2003.